


Spring 2018

Producing smooth flow in atom circuits by stirring

Olatunde Oladehin

Follow this and additional works at: <https://digitalcommons.georgiasouthern.edu/etd>

 Part of the [Atomic, Molecular and Optical Physics Commons](#), [Condensed Matter Physics Commons](#), and the [Quantum Physics Commons](#)

Recommended Citation

Oladehin, Olatunde, "Producing smooth flow in atom circuits by stirring" (2018). *Electronic Theses and Dissertations*. 1721.

<https://digitalcommons.georgiasouthern.edu/etd/1721>

This thesis (open access) is brought to you for free and open access by the Graduate Studies, Jack N. Averitt College of at Digital Commons@Georgia Southern. It has been accepted for inclusion in Electronic Theses and Dissertations by an authorized administrator of Digital Commons@Georgia Southern. For more information, please contact digitalcommons@georgiasouthern.edu.

PRODUCING SMOOTH FLOW IN ATOM CIRCUITS BY STIRRING

by

OLATUNDE OLADEHIN

(Under the Direction of Mark Edwards)

ABSTRACT

We studied how smooth flow can be produced by stirring an ultracold atom circuit consisting of a gaseous Bose–Einstein condensate (BEC) confined in a “racetrack” potential. The racetrack potential was made up of two straight parallel channels of length L connected on both ends by semicircular channels of the same width and (energy) depth as the straight-aways. We used the Gross–Pitaevskii equation to simulate the behavior of the BEC in this potential when stirred by a rectangular paddle at various speeds and barrier heights. We found that smooth flow could be produced and conducted a systematic study of the flow produced under various conditions. We also laid the groundwork for the development of a simple model of the stirring of the BEC. This understanding should enable the design of a stirring sequence that would produce a given flow on demand.

INDEX WORDS: Bose–Einstein condensate, Atom circuit, Smooth flow

PRODUCING SMOOTH FLOW IN ATOM CIRCUITS BY STIRRING

by

OLATUNDE OLADEHIN

B.S, University Of Ibadan, Nigeria, 2014

A Thesis Submitted to the Graduate Faculty of Georgia Southern University in Partial

Fulfillment

of the Requirements for the Degree

MASTER OF SCIENCE

STATESBORO, GEORGIA

©2018

OLATUNDE OLADEHIN

All Rights Reserved

PRODUCING SMOOTH FLOW IN ATOM CIRCUITS BY STIRRING

by

OLATUNDE OLADEHIN

Major Professor: Mark Edwards

Committee: Clayton Heller

Maxim Durach

Electronic Version Approved:

May 2018

DEDICATION

This thesis is dedicated to my beloved parents and family for their endless love, support and encouragement.

ACKNOWLEDGMENTS

I would first like to thank my thesis advisor Dr. Mark Edwards for his continuous support of my master study and research, for his motivation, encouragement, and vast knowledge. His advice helped me in all the time of research and writing of the thesis.

Besides my advisor, I would like to thank the rest of my thesis committee: Dr. Clayton Heller, Dr. Maxim Durach, for their support and heartening, intuitive comments.

My genuine thanks also go to my fellow researchers: Ben Heller, Colson Sapp for their assistance. Also I thank my friend Femi-Oyetero John for his support during the course of my program.

Finally, I must express my profound gratitude to my parents Mr and Mrs Oladehin and to my siblings for providing me unfailing support and continuous encouragement throughout the years of study and through the process of researching writing this thesis. This accomplishment would not have been possible without them. I really appreciate their effort and prayers. Thank you

TABLE OF CONTENTS

ACKNOWLEDGMENTS	3
LIST OF FIGURES	7
LIST OF TABLES	12
1 Introduction	13
1.1 Atomtronic Systems	13
1.2 Atom Circuit Technology	14
1.3 Example Atom Circuit: Rotation Sensor	16
1.4 Plan of the Thesis	18
2 Background Material	21
2.1 Quantum Mechanics of Many–Body Systems	21
2.2 What is a Bose–Einstein Condensate?	23

	5
2.3 Derivation of the Gross–Pitaevskii Equation	25
2.4 The signature of smooth flow	29
2.4.1 The condensate velocity distribution	30
2.5 Optical Potentials and Atom Circuits	31
2.5.1 Atom circuit optical potential	34
3 Atom Circuit Stirring Study	36
3.1 The racetrack potential	37
3.2 Stirring with an elliptical barrier	39
3.2.1 Elliptical barrier potential	39
3.2.2 Case (1): stir fast with strong barrier	41
3.2.3 Case (2): stir slower with strong barrier	44
3.2.4 Case (3): speed ramp with strong barrier	46
3.2.5 Case (4): speed ramp with weak barrier	48
3.2.6 Case (5): speed ramp, ramp down barrier	50
3.3 Stirring with a rectangular barrier	52

	6
3.3.1	Choosing simulation parameters 53
3.3.2	Can the rectangular barrier make smooth flow? 56
3.4	Systematic study methodology 59
3.4.1	Simulation parameter space 59
3.4.2	Simulation computational details 62
3.5	Systematic study results and analysis 64
3.6	Condensate behavior along the racetrack midline 82
4	Summary 85
REFERENCES 87
A	The ground–state energy functional 92
B	Condensate Velocity Distribution 95
B.1	Lab frame velocity distribution 95
B.2	Rotating frame velocity distribution 98

LIST OF FIGURES

Figure Figure 1.1	Sequence of the operation of an idealized atom circuit designed for rotation sensing. A BEC is formed in the racetrack potential (top left); stirred (top middle) to create smooth flow (top right); a new circuit element is morphed on (bottom right); readout is accomplished by non-destructive imaging (bottom middle); and the device is reset by stopping the flow with a barrier (blue rectangle, bottom left) and the sequence repeats.	17
Figure Figure 2.1	Our typical atom-circuit setup consists of a red-detuned light sheet to provide strong harmonic confinement of the atoms into a horizontal plane combined with an arbitrary planar potential.	34
Figure Figure 3.1	The racetrack atom-circuit potential has two parallel channels of length L and capped by two semi-circular channels of inner radius R_1 and outer radius R_2 . The potential is zero inside the track and V_0 outside.	37

- Figure Figure 3.2 Optical density for Case (1). Racetrack parameters: $V_0 = 500$ nK, $L = 60 \mu\text{m}$, $R_1 = 15 \mu\text{m}$, $R_2 = 25 \mu\text{m}$; Vertical confinement parameter: $\omega_z = 2\pi \times (500\text{Hz})$; Barrier and Stir parameters: $V_p = 500$ nK, $\Omega = 2\pi \times (30\text{Hz})$ 41
- Figure Figure 3.3 Optical density for Case (2). Racetrack parameters: $V_0 = 500$ nK, $L = 60 \mu\text{m}$, $R_1 = 15 \mu\text{m}$, $R_2 = 25 \mu\text{m}$; Vertical confinement parameter: $\omega_z = 2\pi \times (500\text{Hz})$; Barrier and Stir parameters: $V_p = 500$ nK, $\Omega = 2\pi \times (6\text{Hz})$ 44
- Figure Figure 3.4 Optical density for Case (3). Racetrack parameters: $V_0 = 500$ nK, $L = 60 \mu\text{m}$, $R_1 = 15 \mu\text{m}$, $R_2 = 25 \mu\text{m}$; Vertical confinement parameter: $\omega_z = 2\pi \times (500\text{Hz})$; Barrier and Stir parameters: $V_p = 500$ nK, $\Omega_{\text{final}} = 2\pi \times (6\text{Hz})$ 46
- Figure Figure 3.5 Optical density for Case (4). Racetrack parameters: $V_0 = 500$ nK, $L = 60 \mu\text{m}$, $R_1 = 15 \mu\text{m}$, $R_2 = 25 \mu\text{m}$; Vertical confinement parameter: $\omega_z = 2\pi \times (500\text{Hz})$; Barrier and Stir parameters: $V_p = 5$ nK, $\Omega_{\text{final}} = 2\pi \times (6\text{Hz})$ 48
- Figure Figure 3.6 Optical density for Case (5). Racetrack parameters: $V_0 = 500$ nK, $L = 60 \mu\text{m}$, $R_1 = 15 \mu\text{m}$, $R_2 = 25 \mu\text{m}$; Vertical confinement parameter: $\omega_z = 2\pi \times (500\text{Hz})$; Barrier and Stir parameters: $V_p = 500$ nK, $\Omega = 2\pi \times (30\text{Hz})$ 50

Figure Figure 3.7 Optical density (left three columns) and phase distribution (right three columns) results of a simulation where a ring BEC under the conditions of Ref. [1] was stirred by a rectangular barrier. Simulation performed by Noel Murray in Edwards Research Group, 2014.	52
Figure Figure 3.8 The stir schedule for all rectangular barrier simulations. The rectangular barrier energy height is ramped up from zero to $V_{p,max}$ over 500 ms, held at $V_{p,max}$ for another 500 ms, and then ramped down to zero over 500 ms. The system is then evolved for a further 2500 ms making the total system evolution time 4000 ms.	54
Figure Figure 3.9 Optical density time sequence for $L = 30 \mu\text{m}$, $\text{TR}=09$, $V_{p,max} = 55 \text{ nK}$	56
Figure Figure 3.10 Phase distribution time sequence for $L = 30 \mu\text{m}$, $\text{TR}=09$, $V_{p,max} = 55 \text{ nK}$	58
Figure Figure 3.11 Examples of optical density, phase distribution, vorticity z -component, and the x and y components of the velocity distribution.	65
Figure Figure 3.12 $L_{00_TR_03}$	68
Figure Figure 3.13 $L_{00_TR_06}$	68
Figure Figure 3.14 $L_{00_TR_09}$	69

Figure Figure 3.15L_00_TR_12	69
Figure Figure 3.16L_10_TR_03	70
Figure Figure 3.17L_10_TR_06	70
Figure Figure 3.18L_10_TR_09	71
Figure Figure 3.19L_10_TR_12	71
Figure Figure 3.20L_20_TR_03	72
Figure Figure 3.21L_20_TR_06	72
Figure Figure 3.22L_20_TR_09	73
Figure Figure 3.23L_20_TR_12	73
Figure Figure 3.24L_30_TR_03	74
Figure Figure 3.25L_30_TR_06	74
Figure Figure 3.26L_30_TR_09	75
Figure Figure 3.27L_30_TR_12	75
Figure Figure 3.28L_40_TR_03	76
Figure Figure 3.29L_40_TR_06	76
Figure Figure 3.30L_40_TR_09	77

Figure Figure 3.31L_40_TR_12	77
Figure Figure 3.32L_50_TR_03	78
Figure Figure 3.33L_50_TR_06	78
Figure Figure 3.34L_50_TR_09	79
Figure Figure 3.35L_50_TR_12	79
Figure Figure 3.36L_60_TR_03	80
Figure Figure 3.37L_60_TR_06	80
Figure Figure 3.38L_60_TR_09	81
Figure Figure 3.39L_60_TR_12	81
Figure Figure 3.40Midline, shown in red, of the racetrack showing where the data from the 3D GPE was extracted.	82
Figure Figure 3.41Plots of the BEC density (red) and the phase (green) at points along the midline in the barrier rest frame. See text for details.	84

LIST OF TABLES

Table Table 3.1	Smooth flow simulations for TR = 3 and 6 revolutions.	62
Table Table 3.2	Smooth flow simulations for TR = 9 and 12 revolutions	63

CHAPTER 1

INTRODUCTION

1.1 Atomtronic Systems

The research project described in this thesis is devoted to studying the feasibility of producing smooth flow in an atom circuit by stirring. An atom circuit is a thin sheet of atomic gas that has been shaped by squeezing it with laser light and cooling it to nearly the absolute zero of temperature. The low temperature of such confined gases enhances the appearance of the wave-like quantum mechanical nature of the constituent atoms so that they form a state called a Bose-Einstein condensate (BEC). A horizontal thin sheet of gas in the BEC state can be molded by the confining laser light into arbitrary closed-loop shapes analogous to closed electric circuits. The gas can then be stirred by lasers so that it flows around the closed loop like the electrons in an electric circuit except that the particles are neutral atoms. The system under study in this work is an example of an atomtronic system.

Atom circuits are examples of “atomtronic” systems which are themselves ultracold-atom systems that are analogs of electronic systems in which neutral atoms instead of electrons flow through the circuit. These systems are of interest because they could potentially be used as quantum simulators, in quantum sensing and computation, and as elements in integrated circuits [2]. As quantum simulators, atomtronic systems can mimic the evolution of other physical systems whose parameters are fixed and which are not easily probed. Examples of such systems include electrons in lattice potentials, Superconducting Quan-

tum Interference Devices (SQUIDs, devices that use the Josephson effect to measure small variations in magnetic flux [3]), and the fractional quantum Hall effect. In contrast to these systems, atomtronic systems can be controlled and probed with exquisite precision [4–13]. Atomtronic systems can be used as quantum sensors with applications in precision navigation and in quantum measurement. These systems can be designed to act as sensors of rotation, magnetic fields, and gravitational fields and these hold the promise of providing a substantial gain in sensitivity over conventional sensing devices [14–21].

Atomtronic integrated circuit applications include radically new types of quantum devices that exploit the phase coherence and persistent currents characteristic of superfluids. Circuit elements such as diodes, transistors, and Josephson junctions have been proposed and some of these have been realized in the laboratory [22–30]. Atom circuits fall into this last category and form the subject of this research project. There are two recent developments that bode well for the future of atom circuits especially for metrological applications.

1.2 Atom Circuit Technology

The last three years has seen a second revolution in the technology of all-optical atom trapping. Starting about ten years ago, several techniques were introduced for the optical confinement of ultracold atoms. These techniques included holographic traps [31, 32], painted potentials [33], and masks [34]. A common setup has been to confine the atoms

in the horizontal planar space between a pair of blue-detuned light sheets and then writing a quasi-2D potential in this plane with a combination of red and blue detuned laser beams [35–39].

The emergence of spatial light modulators (SLM) and digital micro-mirror devices [40] (DMDs) in the last several years is again causing a sea change in the ability of experimentalists to manipulate atoms optically. These devices consist of millions of individually addressable mirrors in a small footprint. The major difference between these devices and the holographic traps, painted potentials, and masks is the ability to produce arbitrary optical potentials which also have arbitrary time dependence. The DMD devices, originally developed for the digital light processing, are capable of 20-KHz full-frame refresh rates and are commercially available at relatively low cost [40]. As theorists, we believe we now have permission to dream up any kind of atom-circuit potential we can think of because now almost anything is possible in the lab.

There has also been a recent experimental breakthrough [41] in preparing number-stabilized ultracold-atom clouds. In the past, the uncertainty in the number of atoms in a Bose-Einstein condensate has typically been 10–20%. This new technique, in which feedback from high-precision Faraday imaging of the cloud performed during the evaporative-cooling process is used to guide subsequent cooling, enables the production of clouds with number uncertainty below the shot-noise limit: $\Delta N < \sqrt{N}$. The capability to apply time-dependent, arbitrary planar potentials to number-stabilized BECs represents a significant boost to the prospects of the field of atomtronics particularly for metrological applications.

As far as we know, there are no labs that currently have both capabilities in place but we believe that it is only a matter of time before this happens. These systems provide an ideal platform for the realization of novel atom circuits.

1.3 Example Atom Circuit: Rotation Sensor

To understand the direction of the overall research effort in atom circuits it is instructive to give an example of how an atom circuit that is part of a practical device might operate. Here we describe the possible operation of such an atom circuit. This sequence is shown in Fig. 1.1. It is important to note that the sequence described here is only an idealized version of how an atom circuit used for a practical application might work.

The cyan-colored oval shown in the figure represents the shape of a channel potential created by laser light to confine a Bose–Einstein–condensed gas. We refer to this potential as the “racetrack” potential which is described in much more detail later in this thesis. We start by making a BEC in the racetrack potential (top left in the figure). The racetrack design was chosen to allow room for stirring operations as well as room for new atom circuit elements to be introduced during the rotation sensing sequence.

After the condensate has been made in the racetrack (top left in the figure), the condensate is stirred with a barrier (red rectangle, top middle) in order to create smooth flow in the condensate. Once smooth flow is obtained (top right), a new circuit element, in the form of a smaller ring with two barriers (red rectangles) and embedded in the lower channel,

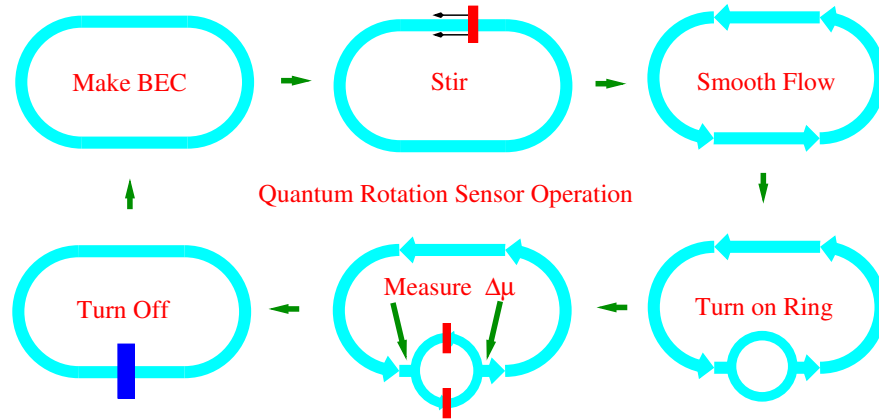


Figure 1.1: Sequence of the operation of an idealized atom circuit designed for rotation sensing. A BEC is formed in the racetrack potential (top left); stirred (top middle) to create smooth flow (top right); a new circuit element is morphed on (bottom right); readout is accomplished by non–destructive imaging (bottom middle); and the device is reset by stopping the flow with a barrier (blue rectangle, bottom left) and the sequence repeats.

is morphed on (easily done with DMD imaging, bottom right in the figure). Measurement readout is accomplished by non–destructive imaging (bottom middle). In this case, if the whole system sits on a platform rotating at speed Ω , the chemical potential difference, $\Delta\mu$, (equal to the BEC density difference) between the left and right sides of the small ring will measure Ω . Finally, the device is reset by either using a potential barrier to stop whatever residual flow is left (bottom left) and stirring again or by making a new condensate.

It is important to mention here that any flow of the condensate will be *quantized*. As will be explained in detail later in the thesis, because the behavior of the BEC is modeled by the Gross–Pitaevskii equation (a nonlinear Schrödinger equation), the velocity distribution is proportional to the gradient of the phase of the condensate wave function. Since the

wave function must be single-valued, it follows that the phase accumulated around a closed loop must be an integral multiple of 2π and thus only discrete smooth-flow velocities will be possible.

It is clear that, for this kind of atom-circuit operation to be implemented, it must be possible for on-demand smooth flow to be created in the condensate by some mechanism. There are several possible methods by which flow could possibly be created. Some candidates for this are (1) spatially modulating the atom-atom interaction of the condensate using an external magnetic field, (2) tilting the plane of the potential away from the horizontal so that there is a component of Earth's gravitational field in the plane, (3) shining laser light on portions of the condensate to create a phase gradient in the condensate wave function, and (4) using laser light to create a barrier that stirs the condensate. If there was a simple model that could predict the amount of flow produced by one of these mechanisms, this would be valuable for the design of an atom circuit devoted to a particular application.

1.4 Plan of the Thesis

This thesis describes a study of the ability of laser-created barriers to produce smooth flow on demand by stirring a Bose-Einstein condensate confined in a racetrack potential. The central questions, some of which are addressed here, are:

- Can stirring a BEC in the racetrack potential actually produce smooth flow? Is it possible to make flow with a barrier of any shape?

- If flow can be made, how does the amount of flow produced depend on the stirring speed and strength (energy height) of the barrier?
- How does the amount of flow produced depend on the shape of the racetrack?
- Is it possible to find a simple model that predicts the amount of flow produced by a given stirring?

We will see in what follows that stirring can produce smooth flow but not all barrier shapes produce flow. We found that stirring with a rectangular-shaped barrier will produce flow but that the amount of flow produced depends on the stir speed, v_s , the barrier strength, $V_{p,\max}$, and racetrack length, L . Based on these preliminary findings we conducted a systematic study of the flow produced for different values of v_s , $V_{p,\max}$, and L . We found that, for a given stirring speed, the amount of flow produced was not a monotonic function of $V_{p,\max}$ and that the quantized flow can jump by more than one unit as the barrier strength is increased.

In Chapter 2 we provide the necessary background for understanding the research study including explaining what a gaseous Bose–Einstein condensate is and describing the standard theory that governs its behavior. We also briefly describe how lasers can manipulate atoms so that they can provide the confining potential in which they move and can stir the condensate. We further write down the potential we assume that atoms are subjected and include a description of the racetrack potential. Finally we derive the connection between the phase of the condensate wave function and the condensate velocity

distribution. Chapter 3 provides the details of the study we conducted to determine if it is possible to make smooth flow in a BEC confined in a racetrack atom circuit. We describe how we were unable to make smooth flow with a rotating elliptically shaped barrier. We also detail how we successfully made smooth flow by stirring with a rectangular barrier oriented perpendicular to the racetrack. Finally we describe how we carried out a study of the flow produced when v_s , $V_{p,\max}$, and L were varied systematically and also give the result of the systematic study. We provide a summary of the work in Chapter 4.

CHAPTER 2

BACKGROUND MATERIAL

In this Chapter we give a brief description of many–body quantum mechanics, describe what a Bose–Einstein condensate is, give a brief derivation of the Gross–Pitaevskii equation (GPE) that is the standard theory governing condensate behavior. We also discuss how laser beams can exert forces on atoms, describe the conditions present in the typical atom circuit setup, and provide a brief description of how the velocity distribution of the condensate is related to the gradient of the condensate wave function phase.

2.1 Quantum Mechanics of Many–Body Systems

In the standard version of quantum mechanics, the state of a quantum system is described by a square–integrable wave function [42]. A measurable quantity, \mathcal{A} , is represented by an operator, \hat{A} , that acts on members of the space of valid quantum mechanical wave functions. These operators are required to be linear and hermitian and to possess a complete set of eigenvectors.

$$\hat{A}\psi_n = a_n\psi_n, \quad n = 1, 2, \dots \quad (2.1)$$

The completeness property of the set of eigenvectors means that this set spans the space of wave functions capable of representing a state of the system. The theory predicts the outcomes of measurements by postulating that the only possible result of a measurement is one of the eigenvalues of the operator associated with the quantity measured. The her-

miticity property of these operators guarantees that its eigenvalues will be real numbers. This is an important attribute of predicted measurement outcomes. If the wave function of the system at the time of measurement is known, the theory can also predict the probability of obtaining a particular eigenvalue, say a_m , when \mathcal{A} is measured.

Another postulate of the theory is that, immediately after the measurement of the quantity \mathcal{A} in which the outcome turns out to be eigenvalue a_m , the wave function of the system is the associated eigenvector, ψ_m . This postulate provides the initial condition for the equation (i.e., the Schrödinger equation) that governs the evolution of the system between measurements.

The equation postulated by quantum mechanics to govern the system evolution between measurements is the time–dependent Schrödinger equation (TDSE). For a system of N identical particles, this equation can be written as

$$i\hbar \frac{\partial}{\partial t} \Psi(\mathbf{r}_1, \dots, \mathbf{r}_N, t) = \hat{H}_{MB} \Psi(\mathbf{r}_1, \dots, \mathbf{r}_N, t), \quad (2.2)$$

where \hat{H}_{MB} is the operator that represents the total energy of the system and is called the Hamiltonian. The Hamiltonian for many–body systems of N identical particles that will be considered in this thesis takes the general form

$$\hat{H}_{MB} = \sum_{j=1}^N \left[-\frac{\hbar^2}{2M} \nabla_j^2 + V(\mathbf{r}_j, t) \right] + \sum_{j < k} V_{\text{int}}(\mathbf{r}_j, \mathbf{r}_k). \quad (2.3)$$

The first term in the Hamiltonian is the sum over the kinetic energies of the individual particles; the second term is the sum over the potential energies of the particles; and the last term represents pairwise interactions and is a double sum over all pairs of particles

with no self–interaction. In modeling interactions in Bose–Einstein–condensed systems, only binary scattering of particles will be considered here.

The wave function solution of the many–body TDSE must also satisfy the normalization condition:

$$\langle \Psi | \Psi \rangle \equiv \int d^3 r_1 \cdots \int d^3 r_N \Psi^*(\mathbf{r}_1, \dots, \mathbf{r}_N, t) \Psi(\mathbf{r}_1, \dots, \mathbf{r}_N, t) = 1. \quad (2.4)$$

Note that the above notation implies integration over all $3N$ –dimensional space. This condition ensures that the sum of the predicted probabilities of outcomes of a particular measurement will be unity.

2.2 What is a Bose–Einstein Condensate?

A gaseous Bose–Einstein condensate is a system of identical bosonic atoms all of whom have the same matter–wave shape (i.e., they have the same single–particle wave function.) The BEC state was first predicted by Albert Einstein and Satyendra Nath Bose, an Indian Physicist [43], in 1925. Bose–Einstein condensation in dilute atomic gases was first achieved by Eric Cornell and Carl Wieman in 1995 and marked the beginning of the development of ultracold quantum gases [44]. For a more in–depth discussion on the theory behind BECs see Ref. [43].

In the quantum theory of angular momentum [42], the square of a particle’s spin angular momentum can only take on the values $j(j+1)\hbar^2$ where the quantum number j can only have either non–negative integer or half–integer values. Elementary particles and ag-

gregates of particles, such as atoms, can be classified into two types: fermions and bosons. Fermions are particles, or aggregates of particles, with half-integer spin while bosons have integer spin. Systems of identical fermions behave differently from systems of identical bosons. The many-body wave function describing a system of identical fermions must obey the Pauli Exclusion Principle. This principle states that, if the coordinate labels (i.e., space and spin) of any two identical fermions are interchanged, the many-body wave function must change its overall sign. The many-body wave function is antisymmetric under particle exchange. If the many-body wave function of a system of N identical fermions can be written as the N -fold product of single-particle orbital functions, then the Pauli Principle can be restated that no two identical fermions can occupy the same single-particle (which may include both space and spin variables) quantum state.

On the other hand, The Pauli Principle requires the many-body wave function for a system of identical bosons to remain unchanged when the space and spin labels of any pair of particles is interchanged. That is, the many-body wave function must be symmetric under particle interchange. In the single-particle view where the many-body wave function is the N -fold product of single-particle orbitals, there is no restriction on the number of bosonic particles that can occupy the same single-particle state. In fact, as will become clear later, bosonic particles in equilibrium prefer to occupy the same single-particle orbital since this is an effective way to lower the total energy of the system.

Atoms are systems of electrons, protons, and neutrons that can exhibit, in aggregate, either bosonic or fermionic character. Electrons, protons, and neutrons are, them-

selves, spin-1/2 fermions. A neutral atom will be either a boson or a fermion depending on whether the total number of electrons, protons, and neutrons is even or odd. According to the rules [42] for adding quantum angular momenta, the total angular momentum of a system of two half-integer angular momenta can only have integer character. Thus, if the total number of electrons, protons, and neutrons in an atom is even, the atom is a boson. If the total number is odd, the atom is a fermion. For example, neutral lithium has two isotopes with large relative abundances: ${}^6\text{Li}$ and ${}^7\text{Li}$. Lithium has atomic number $Z = 3$ which counts the number of protons and the superscripted number is the nucleon number which counts the total number of protons and neutrons. Thus neutral ${}^6\text{Li}$ has three protons, three neutrons, and three electrons making a total of nine particles. This makes ${}^6\text{Li}$ a fermionic atom. On the other hand ${}^7\text{Li}$ has one more neutron for a total of ten particles and so ${}^7\text{Li}$ is a boson.

2.3 Derivation of the Gross–Pitaevskii Equation

In this section, in order to provide a better understanding of the assumptions of the underlying description of gaseous Bose–Einstein condensates, we present a derivation of the time-independent Gross–Pitaevskii equation. Much of the results presented in this thesis was obtained using the *time-dependent* Gross–Pitaevskii equation. However, the basic assumptions for the time-dependent GPE are the same while the derivation is more mathematically complicated and tends to obscure the main points we want to convey to the reader. Even here some of the technical details have been relegated to an appendix. The

time-independent GPE can be derived at various levels of sophistication and these can be found in many places in the literature [43, 45]. The derivation presented here is after the one in Ref. [43].

The standard theory governing the behavior of the Bose–Einstein condensate is the time-dependent Gross–Pitaevskii Equation. The GPE describes the ground state of a quantum system of identical bosons using the Hartree–Fock approximation and the contact interaction model [46]. To reach the Bose–Einstein condensate state, a dilute gas of bosons is cooled close to absolute zero [47, 48] and so the many-body ground state can be assumed to be that in which all of the N bosons occupy the same single-particle quantum state.

The time-independent GPE can be derived using the variational approximation method where the trial wave function is assumed to be the N -fold product of a single single-particle “condensate wave function,” $\phi(\mathbf{r})$. Under this assumption, the many-body wave trial function thus has the form

$$\Psi_{\text{MB}}(\mathbf{r}_1, \mathbf{r}_2, \dots, \mathbf{r}_N) = \prod_{i=1}^N \phi(\mathbf{r}_i). \quad (2.5)$$

with the constraint that the condensate wave function, $\phi(\mathbf{r})$ is normalized to unity:

$$\int |\phi(\mathbf{r})|^2 d^3r = 1. \quad (2.6)$$

To carry out the variational procedure we compute the many-body ground-state energy, $E[\phi]$, using the trial wave function and then minimize this energy by allowing arbitrary variations of ϕ subject to the normalization constraint.

The Hamiltonian for this many-body system contains terms for the kinetic and

potential energy of each atom plus a term that describes pairwise interaction among the atoms. It has the form

$$H_{\text{MB}} = \sum_{i=1}^N \left(-\frac{\hbar^2}{2M} \nabla_i^2 + V(\mathbf{r}_i) \right) + \sum_{i<j} V_{\text{int}}(\mathbf{r}_i, \mathbf{r}_j) \quad (2.7)$$

where the interaction is modeled as binary scattering with a contact interaction.

$$V_{\text{int}}(\mathbf{r}_i, \mathbf{r}_j) = g\delta(\mathbf{r}_i - \mathbf{r}_j). \quad (2.8)$$

The atom–atom interaction strength is given by

$$g = \frac{4\pi\hbar^2 a_s}{M} \quad (2.9)$$

where M is the mass of a condensate atom and a_s is the s -wave (i.e. for head–on collisions) scattering length. This interaction model is valid only when the atoms are cold and the gas is dilute. Under these conditions the spacing between atoms is much larger than the scattering length but smaller than their de Broglie wavelength.

The variational approximation method determines the defining equation for the unknown condensate wave function by minimizing the ground–state energy functional with respect to the unknown condensate wave function orbital, $\phi(\mathbf{r})$

$$E[\phi] \equiv \langle \Psi_{\text{MB}} | H_{\text{MB}} | \Psi_{\text{MB}} \rangle \quad (2.10)$$

subject to the constraint that $\phi(\mathbf{r})$ be normalized to unity. The details of calculating this quantity can be found in Appendix A. This result is

$$E[\psi] = \int d^3r \left(-\frac{\hbar^2}{2M} |\nabla\psi(\mathbf{r})|^2 + V(\mathbf{r})|\psi(\mathbf{r})|^2 + \frac{1}{2}g|\psi(\mathbf{r})|^4 \right) \quad (2.11)$$

where $\psi(\mathbf{r}) \equiv N^{1/2}\phi(\mathbf{r})$ and N is the number of condensate atoms.

To find the optimal form of $\psi(\mathbf{r})$, we minimize the energy above with respect to independent variation of $\psi(\mathbf{r})$ and its complex conjugate $\psi^*(\mathbf{r})$ subject to the condition that the total number of particles is

$$N = \int d^3r |\psi(\mathbf{r})|^2 \quad (2.12)$$

Using a Lagrange multiplier to account for the constraint $\delta E - \mu \delta N = 0$ where μ is the chemical potential. This ensures that the particle number remains fixed so that the variation of $\psi(\mathbf{r})$ and $\psi^*(\mathbf{r})$ may thus be arbitrary. This procedure is equivalent to minimizing the quantity $E - \mu N$ at fixed μ .

Letting $\psi^*(\mathbf{r})$ vary arbitrarily as $\psi^*(\mathbf{r}) \rightarrow \psi^*(\mathbf{r}) + \delta\psi^*(\mathbf{r})$ we require the variation of $E - \mu N$ with respect to $\psi^*(\mathbf{r})$ to vanish. Define

$$A[\psi^*(\mathbf{r})] = E[\psi^*(\mathbf{r})] - \mu N[\psi^*(\mathbf{r})] \quad (2.13)$$

then we require that

$$A[\psi^*(\mathbf{r}) + \delta\psi^*(\mathbf{r})] - A[\psi^*(\mathbf{r})] = 0. \quad (2.14)$$

Using Eq. (2.11) we have

$$\left\{ \int d^3r \left[-\frac{\hbar^2}{2M} \nabla^2 (\psi^*(\mathbf{r}) + \delta\psi^*(\mathbf{r})) \psi(\mathbf{r}) + V(\mathbf{r})(\psi^*(\mathbf{r}) + \delta\psi^*(\mathbf{r})) \psi(\mathbf{r}) \right] \frac{g}{2} (\psi^*(\mathbf{r}) + \delta\psi^*(\mathbf{r}))^2 \psi^2(\mathbf{r}) - [\mu \int d^3r (\psi^*(\mathbf{r}) + \delta\psi^*(\mathbf{r})) \psi(\mathbf{r})] \right\} \left\{ \int d^3r \left[-\frac{\hbar^2}{2M} \nabla^2 \psi^*(\mathbf{r}) \psi(\mathbf{r}) + V(\mathbf{r}) \psi^*(\mathbf{r}) \psi(\mathbf{r}) \right] \frac{g}{2} \psi^{*2}(\mathbf{r}) \psi^2(\mathbf{r}) - \mu \int d^3r \psi^*(\mathbf{r}) \psi(\mathbf{r}) \right\} \quad (2.15)$$

Expanding Eq. (2.15) to first order in $\delta\psi^*$ we have

$$\int d^3r \delta\psi^*(\mathbf{r}) \left(-\frac{\hbar^2}{2M} \nabla^2 \psi(\mathbf{r}) + V(\mathbf{r})\psi(\mathbf{r}) + g|\psi(\mathbf{r})|^2\psi(\mathbf{r}) - \mu\psi(\mathbf{r}) \right) = 0 \quad (2.16)$$

yields the time-independent GPE

$$-\frac{\hbar^2}{2M} \nabla^2 \psi(\mathbf{r}) + V(\mathbf{r})\psi(\mathbf{r}) + g|\psi(\mathbf{r})|^2\psi(\mathbf{r}) = \mu\psi(\mathbf{r}) \quad (2.17)$$

Where in the above equation, M is the mass of a condensate atom, \hbar is Planck's constant, V is the potential to which the condensate atoms are subjected. The solution, $\psi(\mathbf{r})$, is the condensate wave function, i.e., the single-particle orbital that all condensate atoms share. The factor μ is the chemical potential which is the energy required to add one more particle to the condensate. The time-dependent version of the GPE, whose solution is denoted by $\Psi(\mathbf{r}, t)$, is given by

$$i\hbar \frac{\partial \Psi}{\partial t} = -\frac{\hbar^2}{2M} \nabla^2 \Psi(\mathbf{r}, t) + V(\mathbf{r}, t)\Psi(\mathbf{r}, t) + gN |\Psi(\mathbf{r}, t)|^2 \Psi(\mathbf{r}, t), \quad (2.18)$$

where here $\Psi(\mathbf{r}, t)$ is normalized to unity.

2.4 The signature of smooth flow

Since the goal of this research project is to investigate whether and how smooth flow can be created in a Bose-Einstein condensate, it is important to define what we mean by smooth flow. Intuitively, the smooth flow is present when the *speed* of the condensate is approximately constant everywhere (although the direction of the velocity may vary in space) and the condensate density is also approximately constant. The question naturally arises as to

how the condensate velocity distribution can be extracted from the condensate wave function. The answer is that, if we write the condensate wave function in terms of its amplitude, $f(\mathbf{r}, t)$, and phase, $\phi(\mathbf{r}, t)$:

$$\Psi(\mathbf{r}, t) \equiv f(\mathbf{r}, t) e^{i\phi(\mathbf{r}, t)}, \quad (2.19)$$

where f and ϕ are real-valued functions, then the velocity distribution is proportional to the gradient of the phase

$$\mathbf{v}(\mathbf{r}, t) = \frac{\hbar}{M} \nabla \phi(\mathbf{r}, t). \quad (2.20)$$

Thus we define the signature of “smooth” flow to be the case when (1) the gradient of the wave function phase is approximately constant and (2) the atom density (given by the square of the wave function) is also approximately constant. In this section we will sketch a derivation of the connection between the velocity distribution and the wave function phase gradient. For clarity some of the details of the derivation will be relegated to an appendix.

2.4.1 The condensate velocity distribution

The condensate velocity distribution can be defined in term of the condensate probability current. If the current is defined to be

$$\mathbf{J}(\mathbf{r}, t) = \frac{\hbar}{2Mi} \left(\Psi^*(\mathbf{r}, t) \nabla \Psi(\mathbf{r}, t) - \Psi(\mathbf{r}, t) \nabla \Psi^*(\mathbf{r}, t) \right) \quad (2.21)$$

and the atom density is defined as $\rho(\mathbf{r}, t) \equiv |\Psi(\mathbf{r}, t)|^2$, then these quantities satisfy a continuity equation

$$\nabla \cdot \mathbf{J}(\mathbf{r}, t) + \frac{\partial \rho(\mathbf{r}, t)}{\partial t} = 0. \quad (2.22)$$

This follows directly from the Gross–Pitaevskii equation. This is a well-known result if the underlying equation is the Schrödinger equation. It is not quite so well known if the underlying equation is the GPE and so the details of this are given in Appendix B.

The condensate velocity distribution, $\mathbf{v}(\mathbf{r}, t)$, can be quantitatively defined in terms of the probability current as

$$\mathbf{J}(\mathbf{r}, t) \equiv \rho(\mathbf{r}, t)\mathbf{v}(\mathbf{r}, t), \quad (2.23)$$

or in terms of $\Psi(\mathbf{r}, t)$ as

$$\mathbf{v}(\mathbf{r}, t) = \frac{\hbar}{2Mi} \left(\frac{\Psi^*(\mathbf{r}, t)\nabla\Psi(\mathbf{r}, t) - \Psi(\mathbf{r}, t)\nabla\Psi^*(\mathbf{r}, t)}{\Psi^*(\mathbf{r}, t)\Psi(\mathbf{r}, t)} \right). \quad (2.24)$$

Now if we insert the phase/amplitude form (Eq. (2.19)) of the condensate wave function into the above expression for the velocity we obtain the following expression for the velocity distribution

$$\mathbf{v}(\mathbf{r}, t) = \frac{\hbar}{M} \nabla\phi(\mathbf{r}, t). \quad (2.25)$$

For full details, see Appendix B. We now have two expressions for the condensate velocity distribution. Equation (2.24), in terms of Ψ , is more convenient for computation while Eq. (2.25) is more useful for presentation and analysis of final results. More discussion of this will be found in Chapter 3.

2.5 Optical Potentials and Atom Circuits

Laser light can be used to exert forces on atoms in a gas. The basic mechanism causing this effect is that the rapidly oscillating electric field produced by the laser beam causes a shift

in the ground state energy of the atom [43] which has the form

$$\Delta E_g = -\frac{1}{2}\alpha(\omega)\langle\mathcal{E}(\mathbf{r},t)^2\rangle_t \quad (2.26)$$

where $\langle\dots\rangle_t$ denotes a time average over the optical period of the laser oscillation. The factor $\mathcal{E}(\mathbf{r},t)$ is the space- and time-dependent envelope of the laser electric field and $\alpha(\omega)$ is the dynamic polarizability of the atom. The polarizability measures the atomic dipole moment induced by the application of an electric field oscillating at optical frequencies. This effect is often called the AC Stark shift or the light shift [49].

When the envelope of the electric field varies in space, as is the case with focused laser beams, the light shift of the ground state causes the atoms to move so as to lower their energy. For alkali atoms, which are the most commonly used atomic species in ultracold atom systems, it is possible to write a simple approximate expression for their polarizability:

$$\alpha(\omega) \approx \frac{|\langle g|\mathbf{d}\cdot\hat{\boldsymbol{\varepsilon}}|e\rangle|^2}{E_e - E_g - \hbar\omega - \frac{1}{2}\hbar\Gamma_e} \quad (2.27)$$

where $\mathbf{d} = -e\mathbf{r}$ is the atomic dipole moment operator, $\boldsymbol{\varepsilon}$ is the polarization vector of the laser light and g denotes the ground state of the atom and e denotes the excited state of the atom quasi-resonantly coupled to the ground state by the laser light. The factor Γ_e is the natural linewidth of excited state e .

The shift of the atom's ground-state energy thus acts like a potential energy for the atom and can be written as

$$V_g(\mathbf{r},t) = -\frac{1}{2}\alpha_r(\omega)\langle\mathcal{E}(\mathbf{r},t)\rangle_t = \frac{\hbar\Omega_R(\mathbf{r},t)^2\delta}{\delta^2 + \frac{1}{4}\Gamma_e^2}, \quad (2.28)$$

where α_r is the real part of the polarizability. The Rabi frequency, given by

$$\Omega_R(\mathbf{r}, t) = |\langle g | \mathbf{d} \cdot \mathcal{E}(\mathbf{r}, t) | e \rangle|, \quad (2.29)$$

is the frequency at which the atom cycles between the ground and excited states due to stimulated absorption and stimulated emission processes. The factor δ , defined as

$$\delta = \omega - (E_e - E_g)/\hbar, \quad (2.30)$$

is the *detuning* from resonance of the laser photon energy. When the detuning, δ , is positive, the energy of the laser photon is greater than the energy difference between the ground and excited state and the laser causes the ground state of the atom to shift upward. In this case, we say that the laser is “blue detuned” with respect to the atomic transition. Atoms tend to move toward the lowest intensity of blue-detuned laser light because this lowers their internal energy. When δ is negative, the energy of the laser photon is less than the energy difference between the ground and excited state of the atom and this causes the ground state of the atom to shift downward. In this case, we say that the laser is “red-detuned” with respect to the atomic transition. Atoms tend to move toward the highest intensity of red-detuned laser light. Thus red- and blue-detuned lasers can be used in combination to confine and manipulate atoms in a gas.

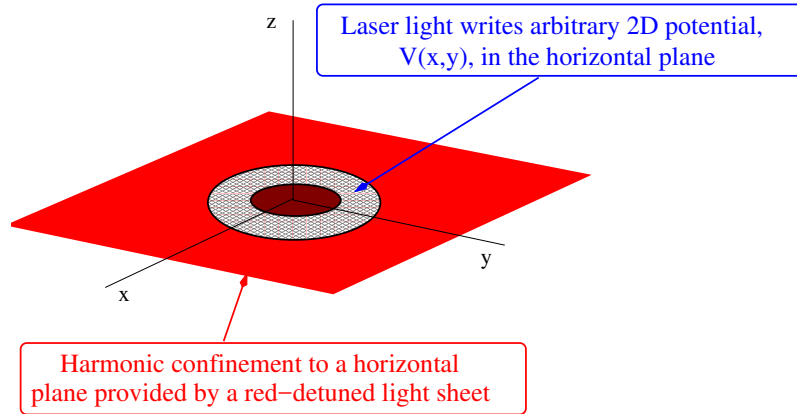


Figure 2.1: Our typical atom-circuit setup consists of a red-detuned light sheet to provide strong harmonic confinement of the atoms into a horizontal plane combined with an arbitrary planar potential.

2.5.1 Atom circuit optical potential

Figure 2.1 shows a cartoon picture of the typical atom-circuit that we are studying in this research project. This setup is typical of many recent atomtronics experiments [35, 36]. It consists of a single red-detuned light sheet (or a pair of parallel blue-detuned light sheets) oriented in a horizontal plane that provides strong confinement of the gas of atoms to this plane. In addition, a digital micro-mirror device (DMD) projects an image onto this plane using red- or blue-detuned light. This image creates a two-dimensional potential with essentially arbitrary dependence on (2D) space and time.

In our model, we take the optical potential experienced by the atoms under these

conditions to have the following general form

$$V(\mathbf{r}, t) = \frac{1}{2}M\omega_z^2 z^2 + V_{\text{ac}}(\mathbf{r}) + V_{\text{stir}}(\mathbf{r}, t). \quad (2.31)$$

Here the first term is the strong vertical harmonic potential of the light sheet that molds the atoms into a thin horizontal sheet of gas. The term V_{ac} represents the potential in the horizontal plane in which the condensate is initially formed and is produced by DMD imaging. In our model, this potential takes the shape of a racetrack. Finally, the term V_{stir} represents the potential barrier that is used to stir the condensate in order to make smooth flow. In our study we consider two stirring potentials, (1) a rotating elliptically shaped barrier centered near one end of the racetrack and (2) a rectangular barrier that is oriented perpendicularly to the racetrack path, is twice the width of the path, and that moves at constant speed along this path. Full details about the racetrack and stirring potentials will be given in Chapter 3.

CHAPTER 3

ATOM CIRCUIT STIRRING STUDY

In this chapter we present our study of whether and how smooth flow can be created in an atom circuit by stirring. The majority of this study consisted of simulations of an atom circuit being stirred for a variety of different cases using the Gross–Pitaevskii equation to model condensate behavior. In all of the simulations, the initial condensate was confined by a trap potential, $V_{\text{trap}}(\mathbf{r})$, with the same basic design. We refer to this as the “racetrack” potential. Within this model we simulated condensate stirring with two different barrier shapes: (1) a rotating elliptical barrier (peristaltic pump) and (2) a rectangular barrier oriented perpendicular to the path of the racetrack.

This plan of this chapter is as follows. In Section 3.1 we describe the racetrack potential in detail and present the parameters that define its shape. In Section 3.2 we describe and present the results of trying to make smooth flow using the rotating elliptical barrier. We were unable to make smooth flow using this barrier shape. In Section 3.3 we describe in detail our attempt to make smooth flow with the rectangular barrier which was successful. This motivated a systematic study of the amount of smooth flow created with rectangular barriers moving at different speeds and having different energy heights and for different racetrack geometries. The details of how the systematic study was conducted are given in Section 3.4. Section 3.5 describes the results of the study. Finally in Section 3.6, we extract from the 3D simulations the behavior of the GPE solution along the 1D midline

of the racetrack potential as a function of time during a single simulation. This enables us to understand better the condensate behavior in the region of the barrier. Furthermore, since the ultimate goal of the stirring study is to develop a simple model for predicting the flow created for given stirring conditions. These results show what a correct 1D model should produce.

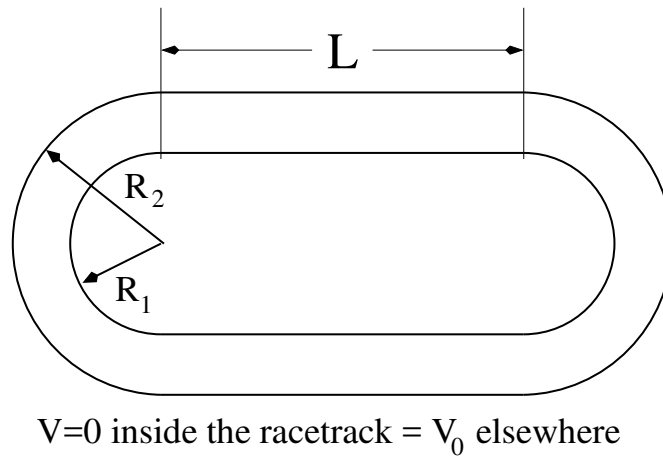


Figure 3.1: The racetrack atom-circuit potential has two parallel channels of length L and capped by two semi-circular channels of inner radius R_1 and outer radius R_2 . The potential is zero inside the track and V_0 outside.

3.1 The racetrack potential

In all of our simulations that follow, we assume that the potential in which the condensate is initially formed is always the same. Thus the condensate present before stirring begins is always the same. This potential consists of a vertical (z direction) harmonic potential with frequency ω_z and a 2D atom-circuit potential defined only in the xy plane. The full initial

potential has the form

$$V_{\text{trap}}(\mathbf{r}) = \frac{1}{2}M\omega_z^2 z^2 + V_{\text{ac}}(\mathbf{r}). \quad (3.1)$$

In our model the atom–circuit, $V_{\text{ac}}(\mathbf{r})$, potential consists of two parallel straight channels of length L connected together at the ends by semicircular channels. This divides the xy plane into a region inside the channel where the potential is equal to zero and outside where it is equal to V_0 . This potential is shown in Fig. 3.1 and we refer to it as the racetrack potential.

The mathematical form of this potential is

$$V_{\text{ac}}(\mathbf{r}) = \frac{1}{2}V_0 \left[\tanh(b(R_1 - \rho(x,y))) + \tanh(b(\rho(x,y) - R_2)) + 2 \right] \quad (3.2)$$

where, $\rho(x,y)$ is given by

$$\rho(x,y) = \left\{ \begin{array}{ll} |y| & |x| \leq \frac{1}{2}L \\ \sqrt{(x + \frac{1}{2}L)^2 + y^2} & x < -\frac{1}{2}L \\ \sqrt{(x - \frac{1}{2}L)^2 + y^2} & x > \frac{1}{2}L \end{array} \right\}. \quad (3.3)$$

This potential steps the potential down from outside to inside the channel and up from inside to outside over a width $1/b$.

The shape of the racetrack potential was motivated by the need to make more room for atom–circuit elements that may be morphed on during operations that might occur after smooth flow is created by stirring (or by whatever means). This can be seen in the rotation sensor example presented in Fig. 1.1 of Chapter 1 where the bottom straight channel was morphed into a channel with a ring in the middle of it. Having the straightaways as long as possible enable flexible design of atom–circuit elements for applications. The first

idea we had for pushing condensate atoms along the channel was to mimic the action of a peristaltic pump.

3.2 Stirring with an elliptical barrier

We tried to mimic how a peristaltic pump works by stirring the racetrack BEC with a rotating elliptical paddle. A peristaltic pump is a positive displacement pump that is used to transfer a wide variety of fluids along a tube. It is based on alternating compression and relaxation of the tube. A pair of rollers alternately pass along the length of the tube totally compressing it and creating a seal between suction and discharge side of the pump.

3.2.1 Elliptical barrier potential

Inspired by this idea we devised a propeller-like barrier that could be located at the center of the semicircles at one end of the racetrack. The elliptical barrier potential has the form:

$$V_{\text{ellipse}}(x, y, x_c, y_c, a, b, \theta(t)) = \left\{ \begin{array}{ll} V_p(t) & [x'(x, y, x_c, y_c, \theta(t))]^2/a^2 + \\ & [y'(x, y, x_c, y_c, \theta(t))]^2/b^2 \leq 1 \\ 0 & [x'(x, y, x_c, y_c, \theta(t))]^2/a^2 + \\ & [y'(x, y, x_c, y_c, \theta(t))]^2/b^2 < 1 \end{array} \right\} \quad (3.4)$$

where

$$\begin{aligned}
 x'(x, y, x_c, y_c, \theta(t)) &= (x - x_c) \cos(\theta(t)) + (y - y_c) \sin(\theta(t)), \\
 y'(x, y, x_c, y_c, \theta(t)) &= -(x - x_c) \sin(\theta(t)) + (y - y_c) \cos(\theta(t)).
 \end{aligned}
 \tag{3.5}$$

In this potential (x_c, y_c) are the coordinates of the fixed center of the rotating barrier, $\theta(t)$ is the angle through which the ellipse must be rotated from its orientation at $t = 0$, and $V_p(t)$ is the energy height of the potential. The shape of the ellipse is defined by the semi-major axis length, a , and the semi-minor axis length, b . The parameters that were adjusted for this potential in the results described below were the ellipse rotation angle function, $\theta(t)$, and the energy height, $V_p(t)$, which can also be a function of time.

We stirred the racetrack BEC with this elliptical barrier in different ways attempting to create smooth flow in the condensate. The barrier stirring was controlled by varying its rotation, $\theta(t)$, and strength, $V_p(t)$, independently. We tried a number of different combinations of these parameters. A selection of different cases are described in detail below. These combinations include, qualitatively, Case (1) stirring fast with a strong barrier, Case (2) stir slower with the same barrier strength, Case (3) ramp up the stir speed from zero over the first half of the simulation, Case (4) same ramp but with a much weaker barrier, and Case (5) ramp up the barrier speed and then ramp off the barrier strength. As will be seen, none of these combinations of parameters were successful in producing smooth flow.

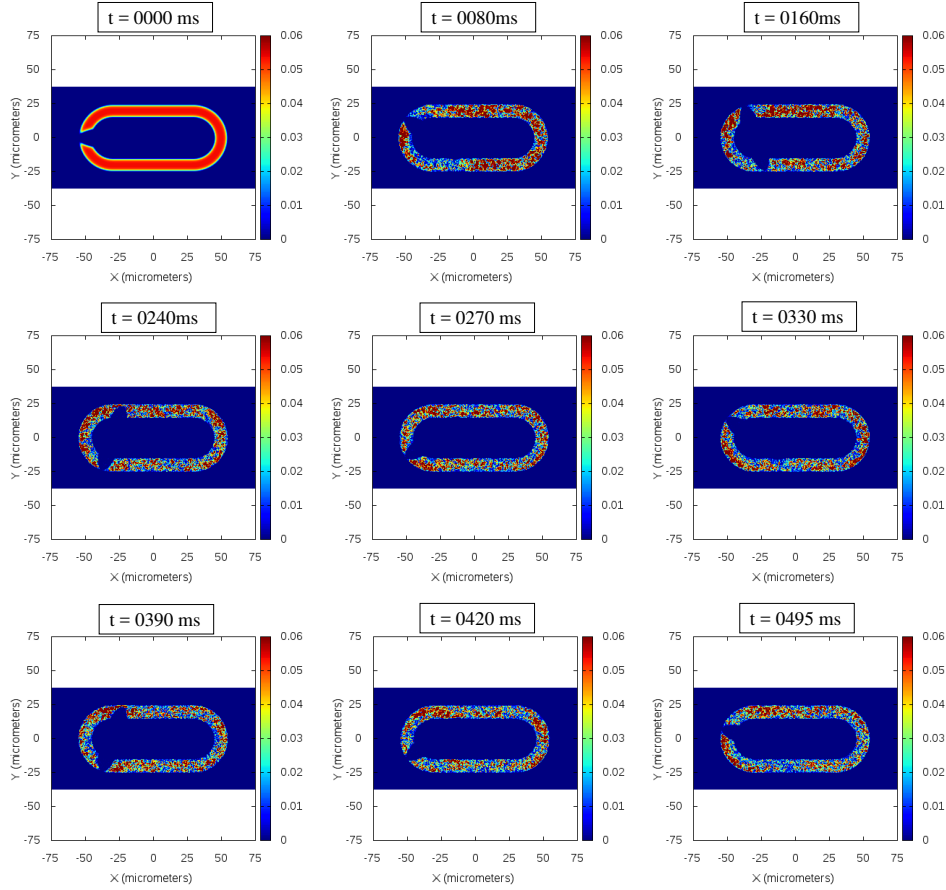


Figure 3.2: Optical density for Case (1). Racetrack parameters: $V_0 = 500$ nK, $L = 60 \mu\text{m}$, $R_1 = 15 \mu\text{m}$, $R_2 = 25 \mu\text{m}$; Vertical confinement parameter: $\omega_z = 2\pi \times (500\text{Hz})$; Barrier and Stir parameters: $V_p = 500$ nK, $\Omega = 2\pi \times (30\text{Hz})$.

3.2.2 Case (1): stir fast with strong barrier

In Case 1 we simulated the stirring of a condensate of $N=500,000$ sodium atoms confined in a racetrack potential of length $L = 60 \mu\text{m}$ and the inner and outer radii were $R_1 = 15 \mu\text{m}$ and $R_2 = 25 \mu\text{m}$, respectively. The frequency of the harmonic potential providing vertical confinement was $\omega_z = 2\pi \times (500\text{Hz})$. The shape of the barrier in this case (and in all subsequent

cases described below) was elliptical with semi-major axis $a = R_2 = 25 \mu\text{m}$ and semi-minor axis $b = R_1 = 15 \mu\text{m}$. The energy height of the ellipse was held fixed at $V_p = 500$ nK and the rotation angle evolved according to $\theta(t) = \Omega t$ where $\Omega = 2\pi \times (30\text{Hz})$. The total evolution time of the simulation was $T_{\text{total}} = 500$ ms.

The results of this simulation are shown in Fig. 3.2. This figure contains nine images. Each image shows a 2D plot of the optical density of the condensate at a fixed time during the system evolution. The tag appearing at the top of each image is the time elapsed since stirring of the condensate began and the images are ordered from left to right starting at the top left.

The 2D optical density of the condensate at point (x, y) in the condensate plane is the total number of atoms contained in a narrow tube of rectangular cross section $(\delta x \times \delta y)$ and oriented perpendicular to the condensate plane. This quantity is computed from the condensate wave function as

$$\rho_{\text{opt}}(x, y, t) \equiv \int_{-\infty}^{+\infty} dz |\Psi(x, y, z, t)|^2. \quad (3.6)$$

This quantity can be compared directly with CCD (charge-coupled device) images taken of condensates in the lab. The images in Fig. 3.2 represent the condensate optical density as a color at each point on a 2D grid of the xy plane containing the condensate.

It is clear from the figure that the result of the stirring in Case (1) does not achieve the smooth flow (or the droids) that we were looking for. In our definition, smooth flow requires approximately constant density and phase gradient. The densities seen here are

turbulent. It is possible that we were stirring too fast. This is addressed by the next case.

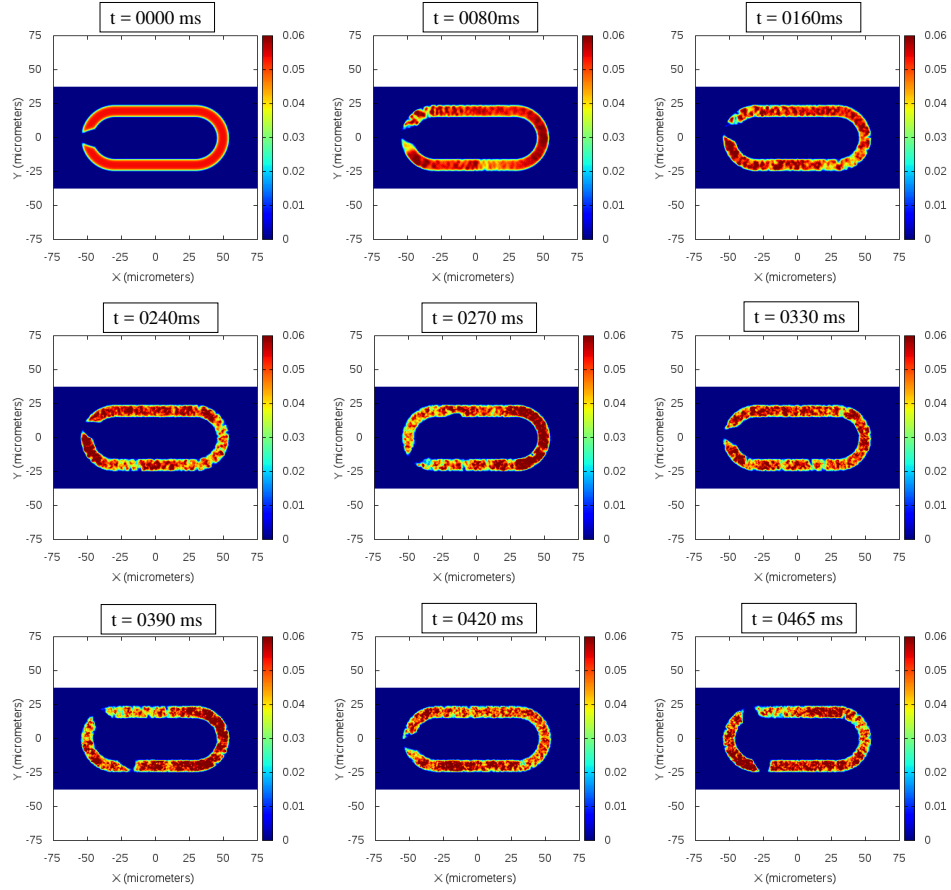


Figure 3.3: Optical density for Case (2). Racetrack parameters: $V_0 = 500$ nK, $L = 60 \mu\text{m}$, $R_1 = 15 \mu\text{m}$, $R_2 = 25 \mu\text{m}$; Vertical confinement parameter: $\omega_z = 2\pi \times (500\text{Hz})$; Barrier and Stir parameters: $V_p = 500$ nK, $\Omega = 2\pi \times (6\text{Hz})$.

3.2.3 Case (2): stir slower with strong barrier

In Case 2 we simulated the stirring of a condensate with the same number of atoms and confining potential as in Case (1). The energy height of the ellipse was again held fixed at $V_p = 500$ nK and the ellipse rotated at a much slower rate, $\theta(t) = \Omega t$ where $\Omega = 2\pi \times$

(6 Hz). The total evolution time of the simulation was again $T_{\text{total}} = 500$ ms.

The results of this simulation are shown in Fig. 3.3 where again nine images of the evolution of the optical density are shown. Comparing this case to Case (1) we see that stirring more slowly does reduce the amount of turbulence created by the barrier but it is still there and the flow is definitely not smooth. Another possible cause of turbulence here is the fact that the barrier is always rotating. We considered the possibility that, if the ellipse rotation was accelerated from zero up to some maximum speed, then this might reduce the turbulence. This possibility is investigated in the Case (3).

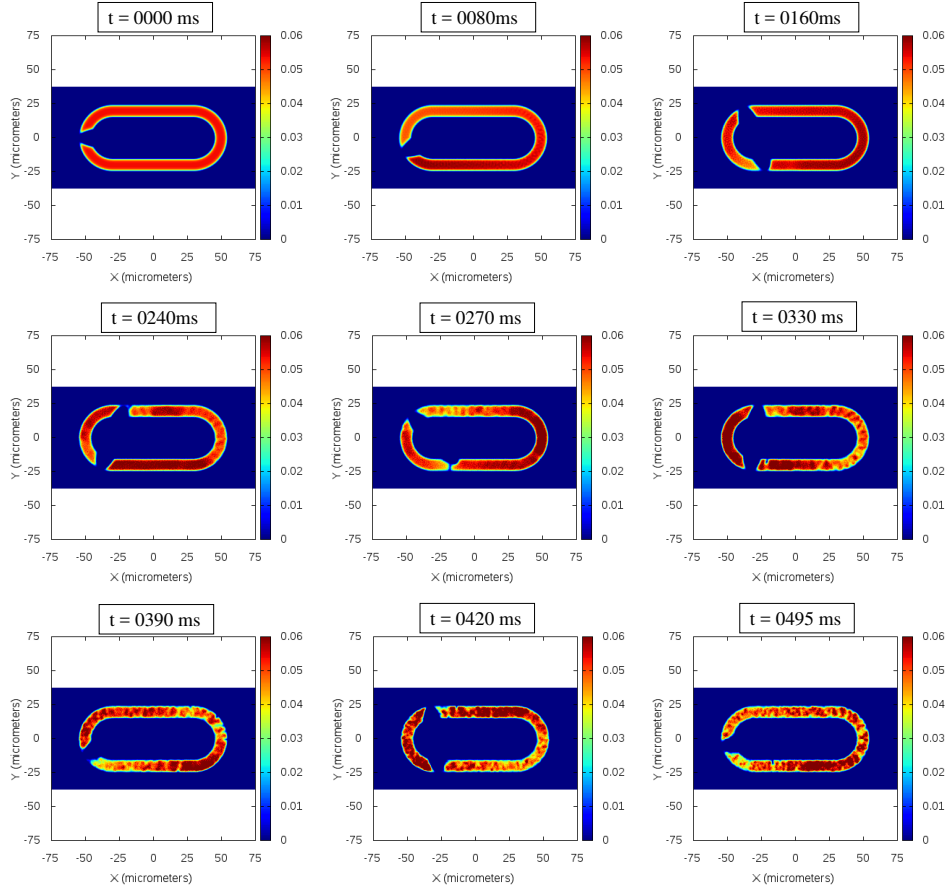


Figure 3.4: Optical density for Case (3). Racetrack parameters: $V_0 = 500$ nK, $L = 60 \mu\text{m}$, $R_1 = 15 \mu\text{m}$, $R_2 = 25 \mu\text{m}$; Vertical confinement parameter: $\omega_z = 2\pi \times (500\text{Hz})$; Barrier and Stir parameters: $V_p = 500$ nK, $\Omega_{\text{final}} = 2\pi \times (6\text{Hz})$.

3.2.4 Case (3): speed ramp with strong barrier

In Case 3 we again simulated the stirring of a condensate with the same number of atoms and confining potential as in Case (1). The energy height of the ellipse was again held fixed at $V_p = 500$ nK and the total evolution time of the simulation was again $T_{\text{total}} = 500$ ms. In

this case, we accelerated the ellipse from 0 Hz to $\Omega_0 = 6$ Hz from $t = 0$ until $t = T = 250$ ms and then kept the rotation speed constant after that. The rotation angle function was thus

$$\theta(t) = 2\pi \times \left\{ \begin{array}{ll} \frac{1}{2} \left(\frac{\Omega_0}{T} \right) t^2 & 0 \leq t \leq T \\ \frac{1}{2} \left(\frac{\Omega_0}{T} \right) T^2 + \Omega_0 (t - T) & t \geq T \end{array} \right\} \text{ radians.} \quad (3.7)$$

The results of this simulation are shown in Fig. 3.4. It clear to see here that the density remains smooth at first but starts to turn turbulent at around $t = 240$ ms. By the end of the simulation there is obvious turbulence and, once again, no smooth flow.

Another possible cause of turbulence here is that the barrier energy height is too strong. In Cases (1), (2), and (3), the barrier height was kept constant at $V_p = 500$ nK which is the same as the depth of the racetrack potential. It is also significantly higher than the chemical potential of the initial condensate. Perhaps, if the barrier height were reduced, then this might get rid of the turbulence. This question is addressed in the next case.

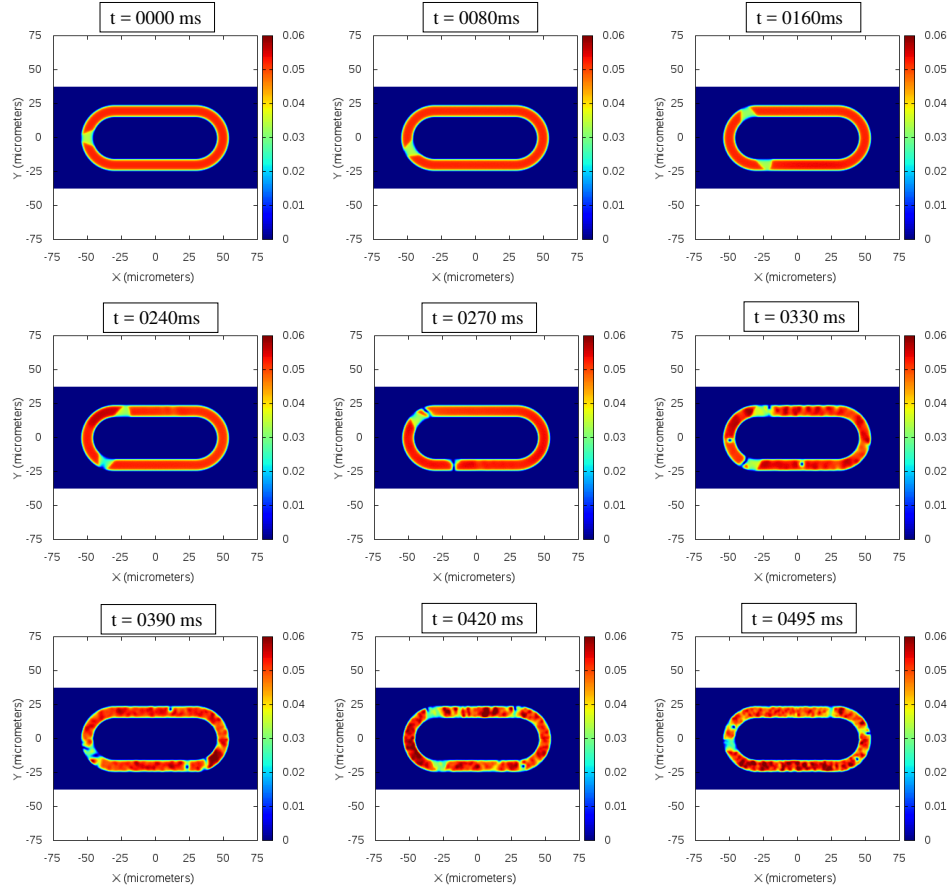


Figure 3.5: Optical density for Case (4). Racetrack parameters: $V_0 = 500$ nK, $L = 60 \mu\text{m}$, $R_1 = 15 \mu\text{m}$, $R_2 = 25 \mu\text{m}$; Vertical confinement parameter: $\omega_z = 2\pi \times (500\text{Hz})$; Barrier and Stir parameters: $V_p = 5$ nK, $\Omega_{\text{final}} = 2\pi \times (6\text{Hz})$.

3.2.5 Case (4): speed ramp with weak barrier

In Case 4 we again simulated the stirring of a condensate with the same number of atoms, confining potential, and stirring schedule (the same $\theta(t)$ as in Eq. (3.7)) as in Case (3). The total evolution time of the simulation was again $T_{\text{total}} = 500$ ms.

In this case the energy height of the ellipse was drastically reduced from $V_p = 500$ nK down to $V_p = 5$ nK, a multiplicative factor of 100. One seemingly major difference between these two barrier strengths is that condensate atoms should be able to tunnel through the barrier.

The results of this simulation are shown in Fig. 3.5. One difference between these results and those of Case (4) is that atoms can now live in the barrier region. Comparing the upper left panels of Fig. 3.4 with that of Fig. 3.5 shows that there is a definite non-zero density in the barrier region initially. The presence of atoms in the barrier region persists throughout the system evolution time. It is also clear however that turbulence is again present under these conditions although it is much reduced even from Case (3) and certainly much less than Case (1).

We made one last change in trying to create smooth flow in the racetrack condensate. This was to add a ramp off of the barrier strength over the last half of the system evolution time. This possibility is addressed in Case (5).

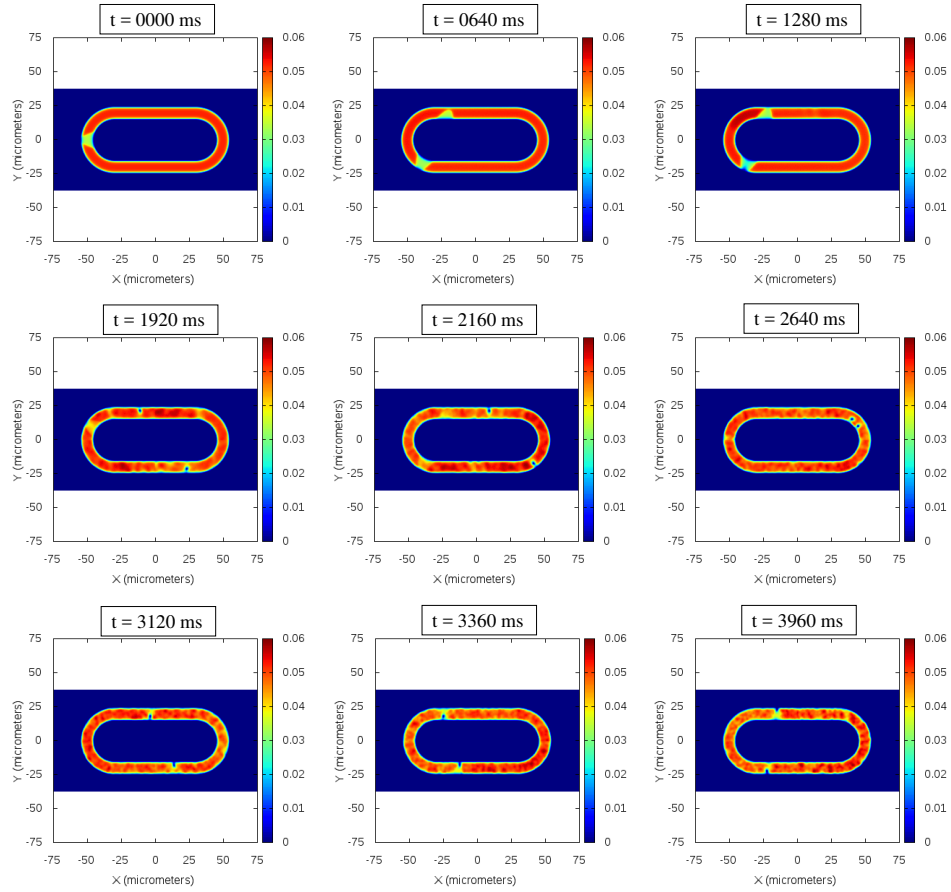


Figure 3.6: Optical density for Case (5). Racetrack parameters: $V_0 = 500$ nK, $L = 60 \mu\text{m}$, $R_1 = 15 \mu\text{m}$, $R_2 = 25 \mu\text{m}$; Vertical confinement parameter: $\omega_z = 2\pi \times (500\text{Hz})$; Barrier and Stir parameters: $V_p = 500$ nK, $\Omega = 2\pi \times (30\text{Hz})$.

3.2.6 Case (5): speed ramp, ramp down barrier

In Case (5) we simulated condensate stirring with the same conditions as Case (4) except that the total system evolution was increased to $T_{\text{total}} = 750$ ms and the energy height of the barrier was ramped from $V_p = 5$ nK down to zero over the last third of the evolution (that

is, from $t = 500$ ms to $t = 750$ ms).

The results of the Case (5) simulation are shown in Fig. 3.6. We once again see that this helps with the reduction of turbulence. It does not remove it however. At this point we concluded that, while it might be possible to create smooth flow using a rotating elliptical barrier in a racetrack condensate, the method would be very difficult to implement. Turbulence was present in all of the simulations we conducted and our goal was to have near-constant density and phase gradient. Thus we decided to try a different stirring mechanism.

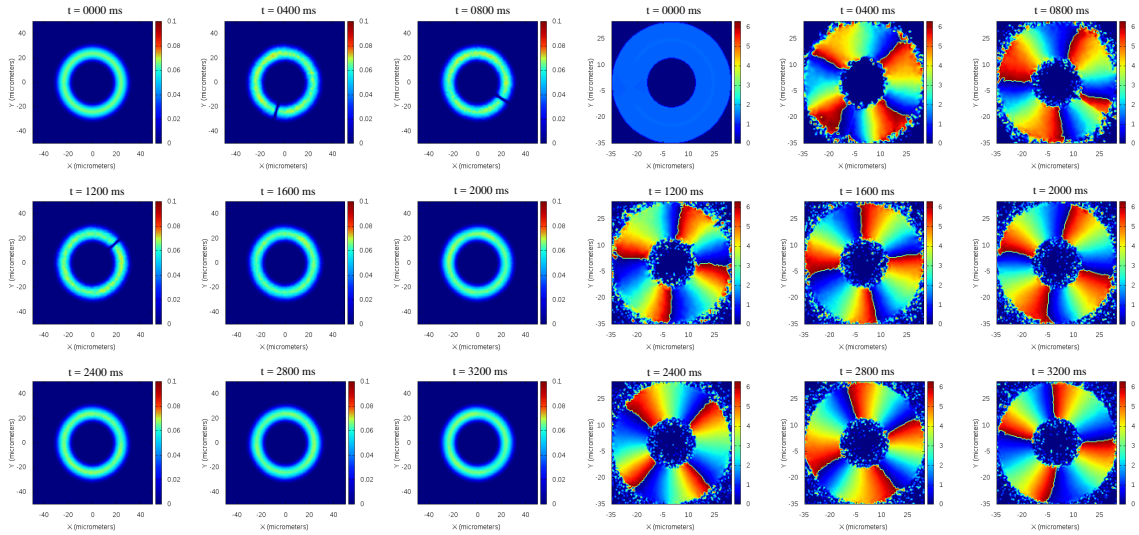


Figure 3.7: Optical density (left three columns) and phase distribution (right three columns) results of a simulation where a ring BEC under the conditions of Ref. [1] was stirred by a rectangular barrier. Simulation performed by Noel Murray in Edwards Research Group, 2014.

3.3 Stirring with a rectangular barrier

The choice of a new stirring barrier was motivated by the fact that we knew that making smooth flow by stirring had already been done for ring-shaped condensates both experimentally and theoretically [1]. In fact simulations where smooth flow was created by stirring a *ring-shaped* condensate with a rectangular barrier oriented perpendicularly to the ring had even been done in the Edwards Research Group some years ago by Noel Murray. Figure 3.7 shows the results of one such simulation where the ring trap conditions matched that of the experiment in Ref. [1]. The figure shows the optical density (left three columns)

and the phase distribution (right three columns) during the stir and afterwards over a period of 3200 ms.

Note that the results of this simulation exhibit the signatures of smooth flow that we defined earlier: approximately constant density and phase gradient. In particular the phase distribution is shown as a color plot where the colors map the phase between 0 (deep blue) and 2π (dark red). Moving along the ring circumference through a rainbow of colors from blue to red represents a 2π advance of the phase along this path. There should always be a whole number of rainbows around the ring because the flow is quantized and, if these rainbows divide the whole path into equal parts (as seen above), this is the signature of smooth flow.

We therefore decided to investigate whether stirring a condensate confined in a racetrack potential that mimiced the ring potential used by Murray with a rectangular barrier would produce smooth flow. It was especially of interest as to whether this type of barrier could produce smooth flow in an elongated racetrack potential.

3.3.1 Choosing simulation parameters

Since the racetrack potential is ring-shaped when $L = 0 \mu\text{m}$, we adjusted the inner and outer radii and the width, b , of the racetrack potential to match the Murray ring potential.

This was a ring harmonic potential

$$V_{\text{murray}}(\rho, z) = \frac{1}{2}M\omega_z^2 z^2 + \frac{1}{2}M\omega_\rho^2 (\rho - \rho_0)^2, \quad (3.8)$$

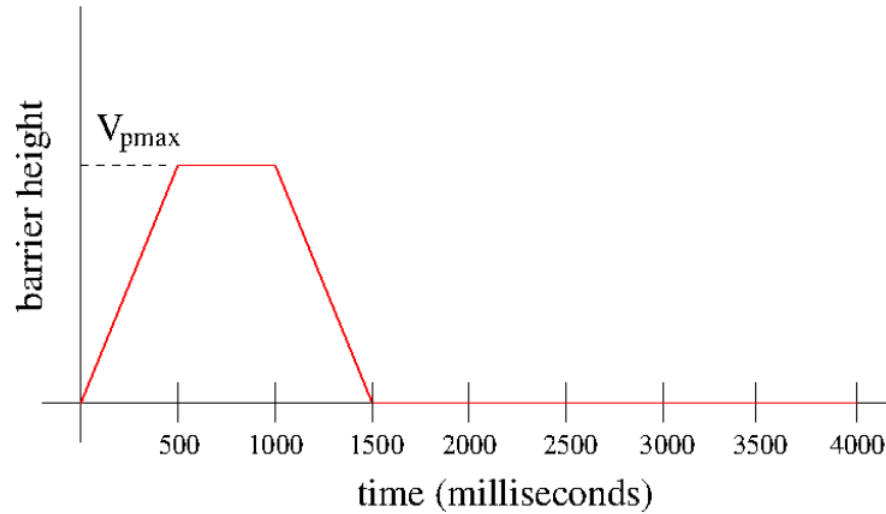


Figure 3.8: The stir schedule for all rectangular barrier simulations. The rectangular barrier energy height is ramped up from zero to $V_{p,max}$ over 500 ms, held at $V_{p,max}$ for another 500 ms, and then ramped down to zero over 500 ms. The system is then evolved for a further 2500 ms making the total system evolution time 4000 ms.

where ρ is the radial cylindrical coordinate. By matching Taylor expansions of the two potentials to second order, we determined the optimal values for the racetrack. These turned out to be $R_1 = 12 \mu\text{m}$, $R_2 = 36 \mu\text{m}$, and $b = 24 \mu\text{m}$. This gives a soft, nearly harmonic cross sectional shape to the channel in the racetrack that matches the Murray ring potential pretty closely. We also chose $\omega_z = 2\pi \times (320\text{Hz})$ and the number of sodium atoms to be $N=500,000$ atoms to match the conditions Murray assumed.

The mathematical form for the rectangular barrier potential is

$$\begin{aligned}
 V_{\text{rect}}(x, y) &= V_p \left(1 \right. \\
 &\quad - V_{\text{up}}(x', -L/2, b) V_{\text{dn}}(x', L/2, b) \\
 &\quad \times V_{\text{up}}(y', -W/2, b) V_{\text{dn}}(y', W/2, b) \left. \right) \tag{3.9}
 \end{aligned}$$

where V_{up} and V_{dn} are up and down step functions:

$$\begin{aligned}
 V_{\text{up}}(x, x_{\text{up}}, b) &= \frac{1}{2} (\tanh(a(x - x_{\text{up}})) + 1) \\
 V_{\text{dn}}(x, x_{\text{dn}}, b) &= \frac{1}{2} (\tanh(a(x_{\text{dn}} - x)) + 1)
 \end{aligned}$$

and

$$\begin{aligned}
 x' &= (x - x_r) \cos(\theta) + (y - y_r) \sin(\theta) \\
 y' &= -(x - x_r) \sin(\theta) + (y - y_r) \cos(\theta).
 \end{aligned}$$

In the above, L and W are the length and width of the rectangle, respectively, (x_r, y_r) are the coordinates of the center of the rectangle, b is the sharpness of the rectangle (small b is a sharp rectangle), and V_p is the energy height of the barrier.

The stirring schedule for the Murray simulation (and all of the simulations presented from here on) is illustrated in Fig. 3.8. The barrier height is ramped up from zero to height $V_{p,\text{max}}$ over 500 ms, held constant at $V_{p,\text{max}}$ for another 500 ms, ramped back down to zero over a further 500 ms, and the system is evolved with the barrier off for another 2500 ms. Thus the total system evolution time is 4000 ms.

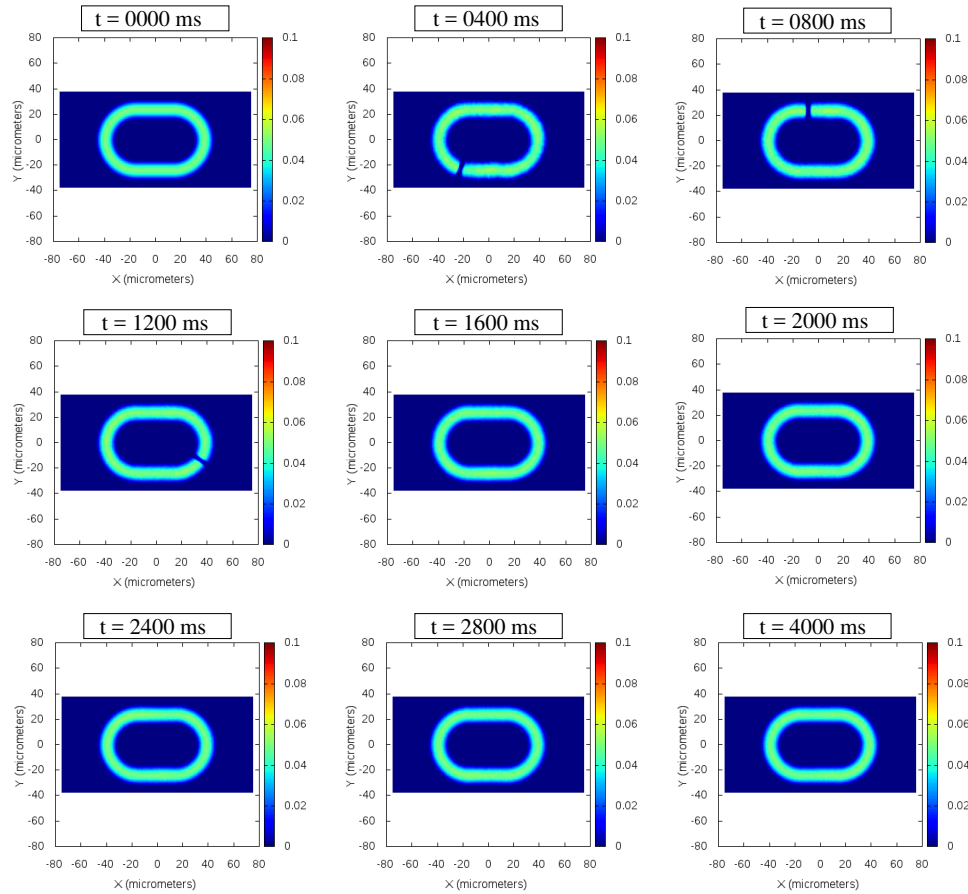


Figure 3.9: Optical density time sequence for $L = 30 \mu\text{m}$, $\text{TR}=09$, $V_{p,\text{max}} = 55 \text{ nK}$

3.3.2 Can the rectangular barrier make smooth flow?

Our attempt to produce smooth flow in a racetrack condensate by stirring with the rectangular barrier oriented perpendicularly to the midline of the racetrack and according to the stirring schedule illustrated in Fig. 3.8 was successful. Figures 3.9 and 3.10 show, respectively, the time sequence of the optical density and the phase distribution for the case where the racetrack length is $L = 30 \mu\text{m}$, the stirring speed was $v = 338 \text{ mm/s}$ and $V_{p,\text{max}} \approx 54 \text{ nK}$.

In Fig. 3.9 we see that the optical density is essentially constant. A closer look will show that there are phonon (sound-wave) ripples on the surface but these are small compared to the bulk density value. The images in this figure start at $t = 0$ and advance by 400 ms each succeeding panel except that the last panel is at the end, $t = 4000$ ms. The middle panel (center row, center column) shows the system just after the end of the stirring. Constant optical density is our first requirement for smooth flow.

The phase density is shown in Fig. 3.10 at the same time tags as in the previous figure. The first four panels (starting at top left) show the evolution while the condensate is being stirred. The flow is clearly evolving with the winding number which is the multiple of 2π through which the phase advances while going around the racetrack (just count the number of red spots). It can be seen to change from zero to three and then to five. After the end of the stirring (middle panel), the winding number never changes. At the end of the simulation (lower right panel), the phase distribution shows that the phase winds through $5 \times (2\pi)$ when we go around the racetrack circumference. We will call this “five units of flow.” These five 2π windings are equally spaced around the racetrack indicating a constant phase gradient which is the second signature of smooth flow.

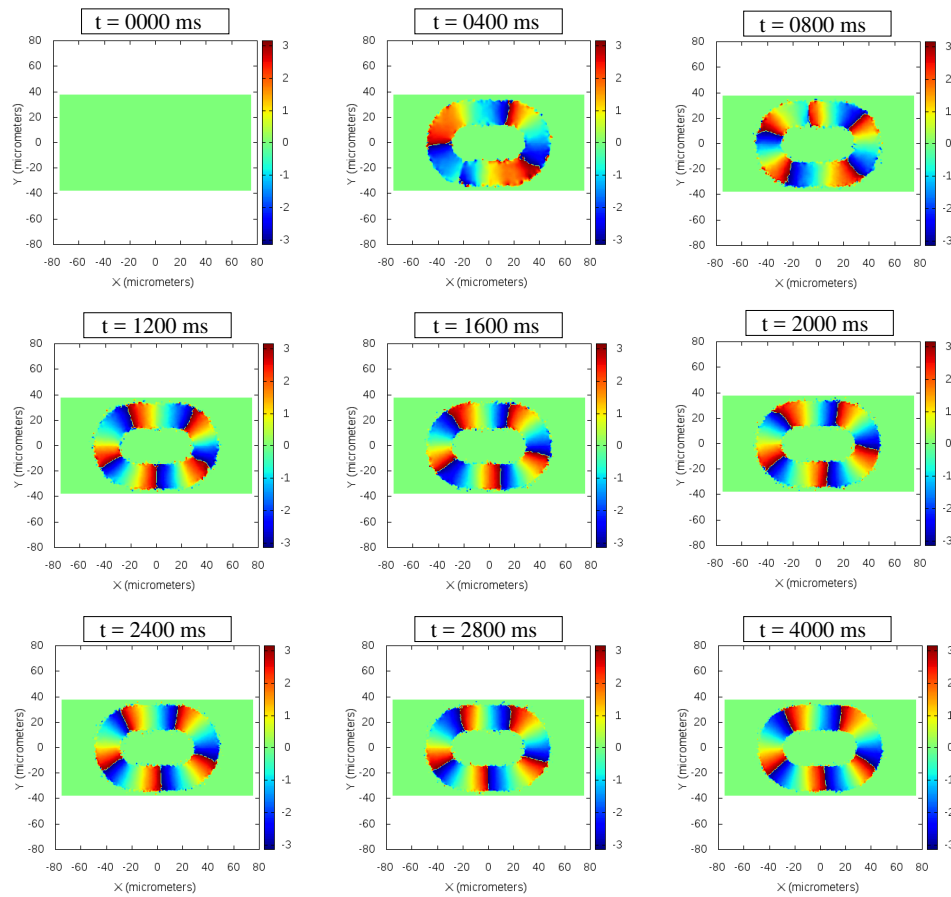


Figure 3.10: Phase distribution time sequence for $L = 30 \mu\text{m}$, $\text{TR}=09$, $V_{p,\text{max}} = 55 \text{ nK}$

Our success in creating smooth by stirring the condensate with the rectangular barrier raised the question: how many units of flow are created if we vary the maximum barrier strength, $V_{p,\text{max}}$, the stirring speed, v_s , and especially the racetrack length, L . Thus we designed and conducted a systematic study of this question. This study consisted of a set of simulations each having different values of the triple of parameters: $(L, V_{p,\text{max}}, v_s)$.

3.4 Systematic study methodology

We studied systematically the ability of the rectangular potential to create smooth flow when used to stir a condensate confined in a racetrack potential. In this study we varied three parameters: (1) L , the racetrack straightaway length, (2) v_s , the stirring speed of the barrier, and (3) $V_{p,\max}$, the maximum value of the barrier energy height during the stir (see Fig. 3.8). Each simulation has a unique set of these three parameters and, in each, the condensate is stirred according to the stirring schedule described earlier and illustrated in Fig. 3.8. In the rest of this section we describe the ranges of the three parameters covered by the collection of simulations carried out in the study. Each simulation required numerical solution of the time-dependent Gross-Pitaevskii equation. Thus we also provide details on how this equation was solved on the computer along with a description of what physical quantities were computed and saved in each simulation.

3.4.1 Simulation parameter space

The parameter space we explored in our set of simulations consisted of seven different racetrack lengths. These were $L = 0, 10, 20, 30, 40, 50,$ and $60 \mu\text{m}$. For fixed L , we stirred the racetrack condensate with a variety of speeds and barrier strengths.

The different speeds sampled in the study were characterized by the number of Total Revolutions (TRs) the barrier would make while circling the $L = 0 \mu\text{m}$ (i.e., the *ring*) racetrack along its midline track during $T_{\text{total}} = 4$ seconds of system evolution time. Four

values of TR were sampled in our study. These were TR = 3, 6, 9, and 12 total revolutions of the ring racetrack. These can be easily translated into speeds, v_s , with more familiar units. The speeds in $\mu\text{m}/\text{second}$ are found by equating the product of the speed, v_s , with the total time, T_{total} , with the product of the Total Revolutions with the circumference of the midline track of the ring racetrack:

$$\begin{aligned} v_s T_{\text{total}} &= (2\pi) \times \frac{1}{2}(R_1 + R_2) \times \text{TR} \quad \text{so,} \\ v_s &= \left(\frac{\pi(R_1 + R_2)}{T_{\text{total}}} \right) \times \text{TR} \equiv v_{s0} \times \text{TR} \end{aligned} \quad (3.10)$$

Since $R_1 = 12 \mu\text{m}$ and $R_2 = 36 \mu\text{m}$, we have $v_{s0} \approx 37.7 \mu\text{m}/\text{s}$ and the four different speeds are 3, 6, 9, and 12 times this basic speed.

For fixed L and TR, we stirred with a number of different maximum barrier strengths, $V_{p,\text{max}}$. This maximum barrier strength was scaled by the chemical potential of the initial condensate and so this scaling parameter will be different for different racetrack lengths, L . The chemical potential is the energy required to add one more atom to the condensate and we calculated this for a condensate with 500,000 sodium atoms confined in the racetrack potential for each of the seven different lengths considered. Calculation of μ can easily be carried out given the wave function of the initial condensate [43].

The maximum barrier strength, $V_{p,\text{max}}$ was varied between 0.5μ and 2.0μ in increments of 0.02μ , that is, 75 different values. A simulation was thus uniquely identified by the values of parameters of racetrack Length, L , Total Revolutions, TR, and maximum barrier strength, $V_{p,\text{max}}$. The full study consists of nearly 2100 separate 3D GPE simulations

of 4000 ms of system evolution time.

We devised a naming system based on these parameters to identify each simulation where L is expressed as the racetrack length in μm , the speed is expressed as the number of TRs, and $V_{p,\text{max}}$ is the maximum barrier height expressed in scaled energy units where each scaled unit is approximately 0.1 nanoKelvin. Thus the identifier “L_30_TR_09_Vpmax_544.7” denotes a length of $L = 30\mu\text{m}$, a speed of $v_s = 3 \times 37.7\mu\text{m/s}$, and $V_{p,\text{max}} \approx 54.5\text{ nK}$. To identify all the simulations with fixed L and TR we would write “L_30_TR_09” for example. Such identifiers label figures given below containing the central result of this thesis. Tables 3.1 and 3.2 summarize the parameter space of our systematic study of smooth-flow production.

L/TR	TR = 3, $v = 112\mu\text{m}/s$	TR = 6, $v = 225\mu\text{m}/s$
$L = 00\mu\text{m}$	$V_{p,\text{max}} = .50\mu, .52\mu, \dots, 2.0\mu$	$V_{p,\text{max}} = .50\mu, .52\mu, \dots, 2.0\mu$
$L = 10\mu\text{m}$	$V_{p,\text{max}} = .50\mu, .52\mu, \dots, 2.0\mu$	$V_{p,\text{max}} = .50\mu, .52\mu, \dots, 2.0\mu$
$L = 20\mu\text{m}$	$V_{p,\text{max}} = .50\mu, .52\mu, \dots, 2.0\mu$	$V_{p,\text{max}} = .50\mu, .52\mu, \dots, 2.0\mu$
$L = 30\mu\text{m}$	$V_{p,\text{max}} = .50\mu, .52\mu, \dots, 2.0\mu$	$V_{p,\text{max}} = .50\mu, .52\mu, \dots, 2.0\mu$
$L = 40\mu\text{m}$	$V_{p,\text{max}} = .50\mu, .52\mu, \dots, 2.0\mu$	$V_{p,\text{max}} = .50\mu, .52\mu, \dots, 2.0\mu$
$L = 50\mu\text{m}$	$V_{p,\text{max}} = .50\mu, .52\mu, \dots, 2.0\mu$	$V_{p,\text{max}} = .50\mu, .52\mu, \dots, 2.0\mu$
$L = 60\mu\text{m}$	$V_{p,\text{max}} = .50\mu, .52\mu, \dots, 2.0\mu$	$V_{p,\text{max}} = .50\mu, .52\mu, \dots, 2.0\mu$

Table 3.1: Smooth flow simulations for TR = 3 and 6 revolutions.

3.4.2 Simulation computational details

Each simulation was carried out by solving the 3D Time–Dependent Gross–Pitaevskii Equation (TDGPE), using the split–step, Crank–Nicolson algorithm [50]. For computational purposes, the GPE was expressed in “scaled” units where the length unit, L_0 , is chosen and the energy unit, E_0 , is defined in terms of L_0 as $E_0 = \hbar^2/(2ML_0)$ and the time unit is $T_0 = \hbar/E_0$. In our case, we took $L_0 = 10^{-5}$ meters or 10 micrometers per scaled length unit.

The parameters used in the numerical solution of the GPE are the number of points in the x grid $N_x = 400$, the number of points in the y grid $N_y = 200$, and the number of points in the z grid $N_z = 50$. The x –grid step size $dx = 3.75 \times 10^{-2}L_0$, the y –grid

L/TR	TR = 9, $v = 338\mu\text{m}/\text{s}$	TR = 12, $v = 450\mu\text{m}/\text{s}$
$L = 00\mu\text{m}$	$V_{p,\text{max}} = .50\mu, .52\mu, \dots, 2.0\mu$	$V_{p,\text{max}} = .50\mu, .52\mu, \dots, 2.0\mu$
$L = 10\mu\text{m}$	$V_{p,\text{max}} = .50\mu, .52\mu, \dots, 2.0\mu$	$V_{p,\text{max}} = .50\mu, .52\mu, \dots, 2.0\mu$
$L = 20\mu\text{m}$	$V_{p,\text{max}} = .50\mu, .52\mu, \dots, 2.0\mu$	$V_{p,\text{max}} = .50\mu, .52\mu, \dots, 2.0\mu$
$L = 30\mu\text{m}$	$V_{p,\text{max}} = .50\mu, .52\mu, \dots, 2.0\mu$	$V_{p,\text{max}} = .50\mu, .52\mu, \dots, 2.0\mu$
$L = 40\mu\text{m}$	$V_{p,\text{max}} = .50\mu, .52\mu, \dots, 2.0\mu$	$V_{p,\text{max}} = .50\mu, .52\mu, \dots, 2.0\mu$
$L = 50\mu\text{m}$	$V_{p,\text{max}} = .50\mu, .52\mu, \dots, 2.0\mu$	$V_{p,\text{max}} = .50\mu, .52\mu, \dots, 2.0\mu$
$L = 60\mu\text{m}$	$V_{p,\text{max}} = .50\mu, .52\mu, \dots, 2.0\mu$	$V_{p,\text{max}} = .50\mu, .52\mu, \dots, 2.0\mu$

Table 3.2: Smooth flow simulations for TR = 9 and 12 revolutions

step size $dy = 3.75 \times 10^{-2} L_0$, and the z -grid step size $dz = 5.0 \times 10^{-2} L_0$. The number of time steps in the propagation was $N_t = 1.375 \times 10^5$ steps, the time-grid step size was $dt = 4 \times 10^{-4} T_0$.

Each simulation produced a 3D space condensate wave function (on a $400 \times 200 \times 50$ -point grid) at each of 100 different times during the 4000 ms system evolution. Each of these wave functions was used to calculate the optical density, the condensate phase in the $z = 0$ plane, the x and y components of velocity field at all grid points in the $z = 0$ plane, and the z -component of the vorticity (curl of the velocity field).

In order to detect the presence of smooth flow we developed diagnostic software suitable for analyzing the results of the GPE simulations of stirred atom circuits. These programs computed the following quantities from each numerically obtained condensate wave function. (Below we use the notation $\Psi(x, y, z, t) = |\Psi(x, y, z, t)| e^{i\phi(x, y, z, t)}$)

- o Optical density: $\rho(x, y, t) = \int_{-\infty}^{\infty} |\Psi|^2 dz$,
- o Velocity x and y components: $v_x = (\hbar/M) \frac{\partial \phi}{\partial x}$ $v_y = (\hbar/M) \frac{\partial \phi}{\partial y}$,
- o Phase distribution: $\phi(x, y, z = 0, t)$
- o Vorticity z component: $\omega_z = \frac{\partial v_y}{\partial x} - \frac{\partial v_x}{\partial y}$.

All of these quantities were computed immediately after calculation of the 100 condensate wave functions which were computed by the GPE solver program and these derived quantities were then saved on a 2D grid. The condensate wave functions, which occupied 100 gigabytes of space on the hard disk, were then deleted. Saving the wave functions would have required 200 Terabytes of space and would still be downloading from the NIST supercomputer, `raritan.nist.gov`, where they computed. Some of the simulations were also performed on the local cluster, `talon.georgiasouthern.edu`. These quantities were used to provide insight into the sometimes complicated behavior of the stirred atom circuit. Figure 3.11 displays examples of each of these quantities. We used the phase distribution to identify how much smooth flow was present at the end of each simulation.

3.5 Systematic study results and analysis

The result of our study was that stirring the racetrack condensate with a rectangular barrier was effective in creating smooth flow. We used the color-map plot of the condensate phase distribution at the end of the system evolution time ($t = 4000$ ms) to study how effective

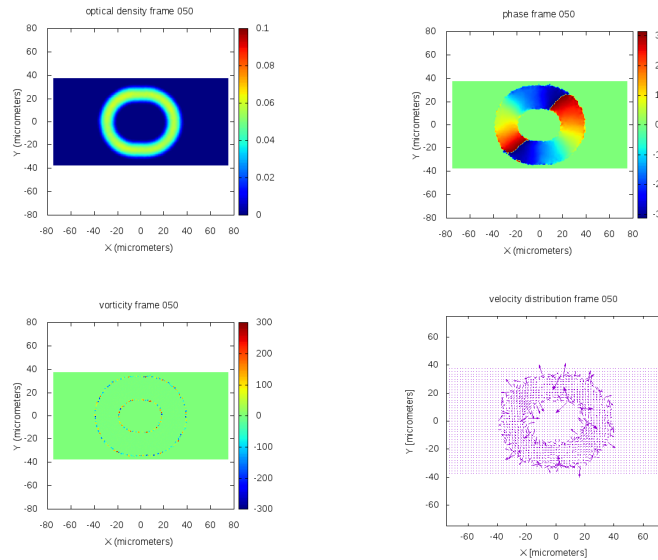


Figure 3.11: Examples of optical density, phase distribution, vorticity z -component, and the x and y components of the velocity distribution.

this stirring was.

These results are shown in Figs. 3.12 through 3.39. Each individual figure shows an aggregation of all of the end-of-simulation phase distribution plots for fixed L and TR . The phase distribution plots in a given figure are ordered from upper left to lower right and the number just above each small plot is the value of $V_{p,max}$ as a fraction of μ , the chemical potential of the initial condensate used in the simulation.

Looking at one of these figures it is easy to see the progression of the flow produced by stirring a condensate at fixed racetrack length and stir speed. The number of flow units produced equals the number of red spots in each small picture. These plots form the central result of this thesis and we will describe some of the interesting features that have

resulted from this study.

This study of smooth-flow production by stirring with a rectangular barrier has revealed some interesting features. These include the following

- Stirring a racetrack condensate with a rectangular barrier does produce smooth flow
- The amount of flow produced by stirring, at fixed L and TR, is not a monotonic function of the barrier strength $V_{p,\max}$. We observed oscillations in the flow produced as $V_{p,\max}$ increases.
- The amount of flow produced by stirring, for fixed L and TR, can jump by more than one as $V_{p,\max}$ increases.
- For weak barriers no flow is produced but, when the barrier is finally strong enough to produce non-zero flow, the amount produced isn't always a single unit of flow.

These features are all present for the case where $L = 30\mu\text{m}$ and TR = 6 total revolutions shown in Fig. 3.25. A close look at this figure shows that, for $0.5\mu \leq V_{p,\max} \leq 0.68\mu$, stirring produces no flow. But then for the next case where $V_{p,\max} = 0.70\mu$, *two units* of flow is produced. This skips over one unit of flow unless this happens in the tiny range of $V_{p,\max}$ between 0.68μ and 0.70μ . From there, after a short stay at two units, it jumps to three units and thereafter jumps back and forth between two units and three units all the way up to $V_{p,\max} = 2.0\mu$ where we stopped doing simulations. Furthermore, there is a large range, $1.5\mu \leq V_{p,\max} \leq 1.78\mu$ where the flow produced remains at two units.

A close look at these graphs shows that this behavior is present to one extent or another in all of the 28 pairs of L and TR included in the study. We concluded that it would be interesting to develop a simple 1D model that could predict how much flow would be obtained under these conditions without having to run a 12-hour 3D GPE simulation every time. To date we have not been able devise such a model. However, we were able to mine the 3D simulations to see what a 1D model ought to get. We now briefly describe the results of this effort.

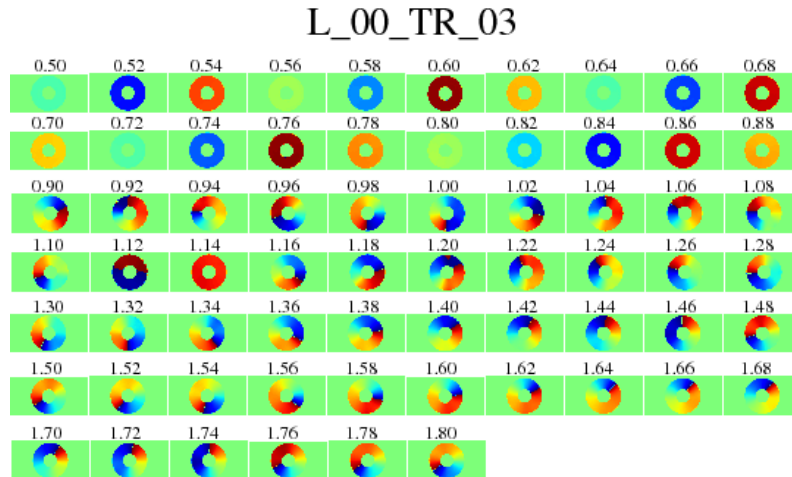


Figure 3.12: L_00_TR_03

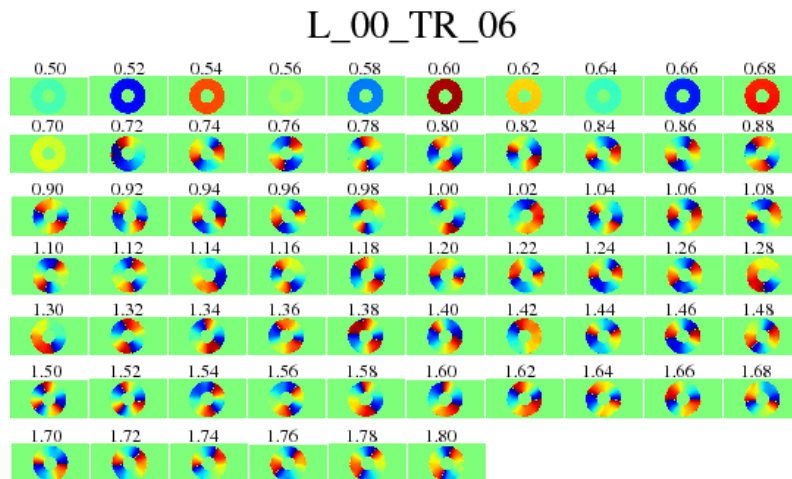


Figure 3.13: L_00_TR_06

L_00_TR_09

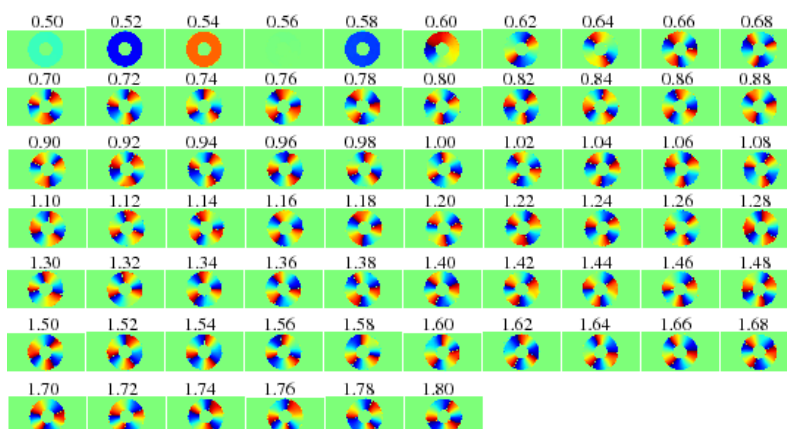


Figure 3.14: L_00_TR_09

L_00_TR_12

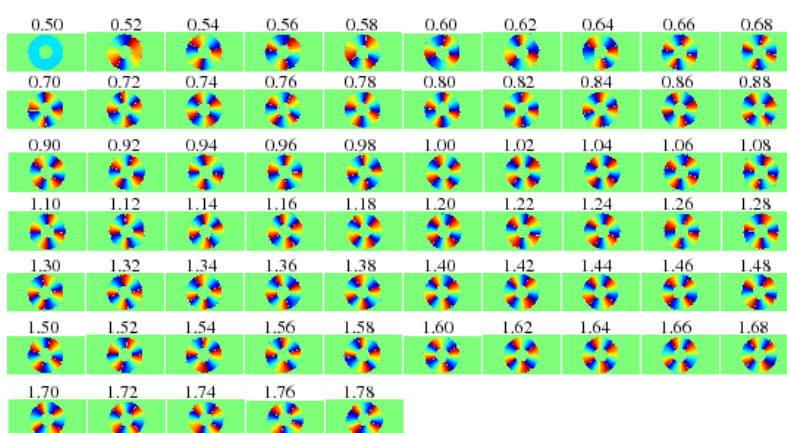


Figure 3.15: L_00_TR_12

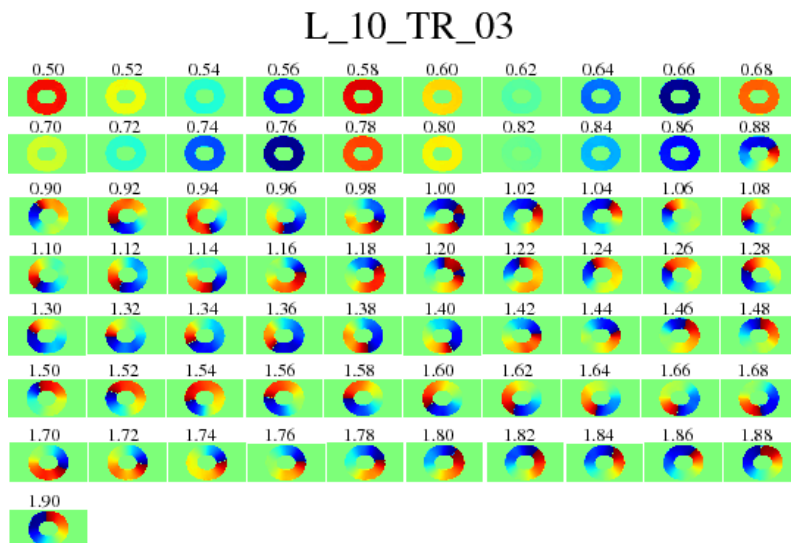


Figure 3.16: L_10_TR_03

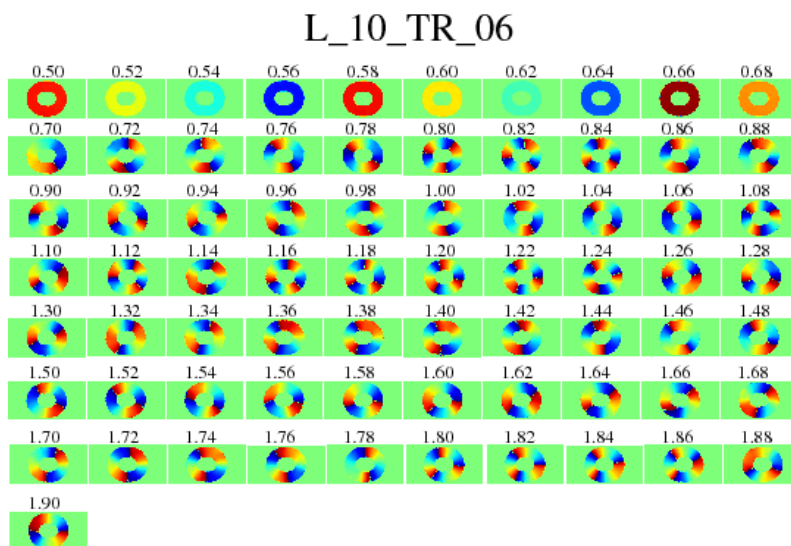


Figure 3.17: L_10_TR_06

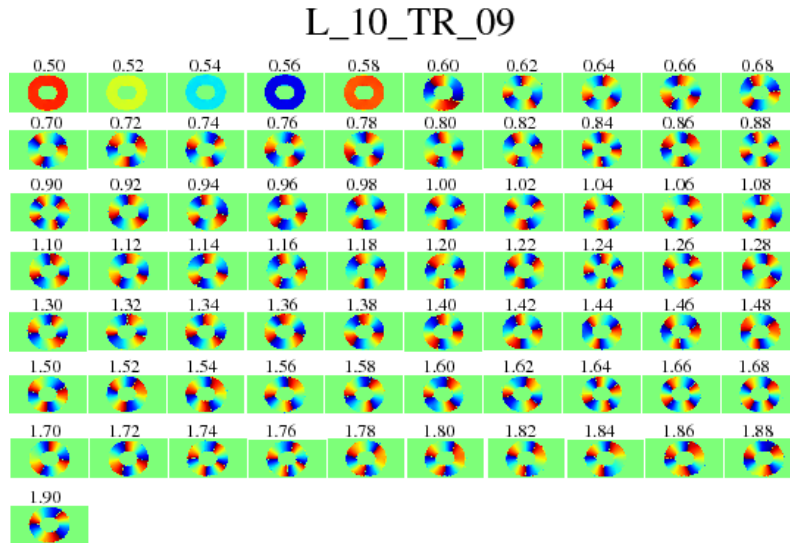


Figure 3.18: L_10_TR_09

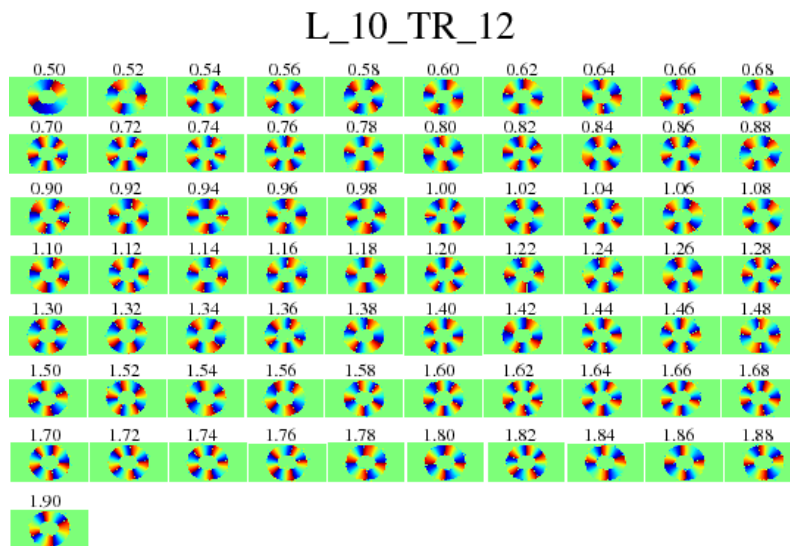


Figure 3.19: L_10_TR_12

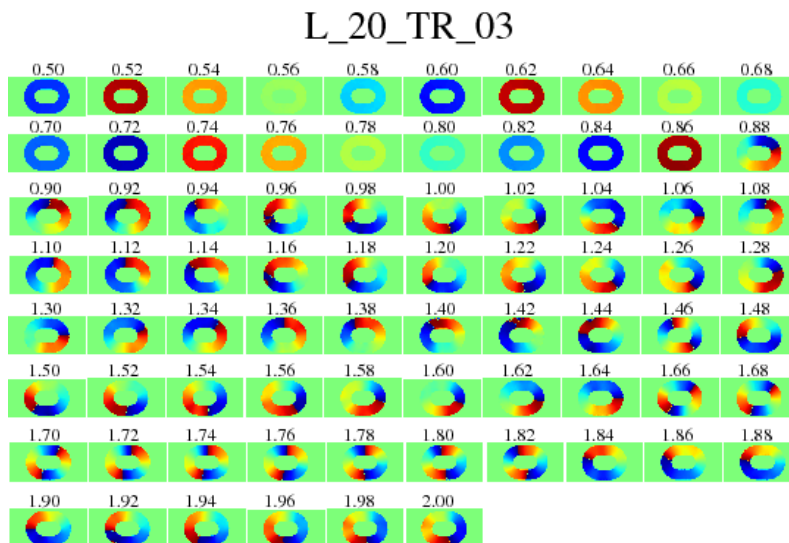


Figure 3.20: L_20_TR_03

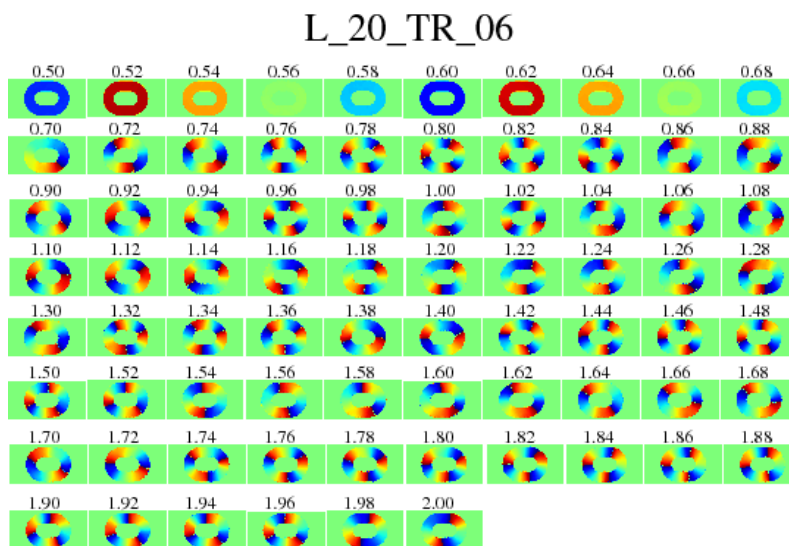


Figure 3.21: L_20_TR_06

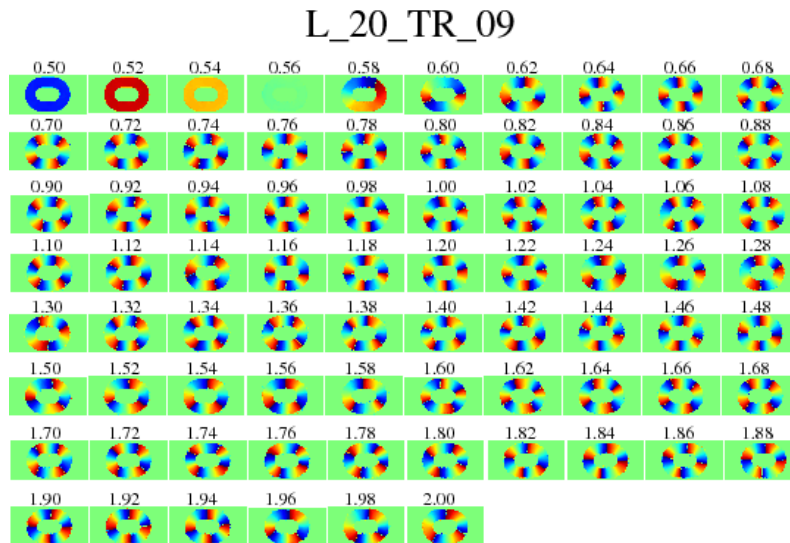


Figure 3.22: L_20_TR_09

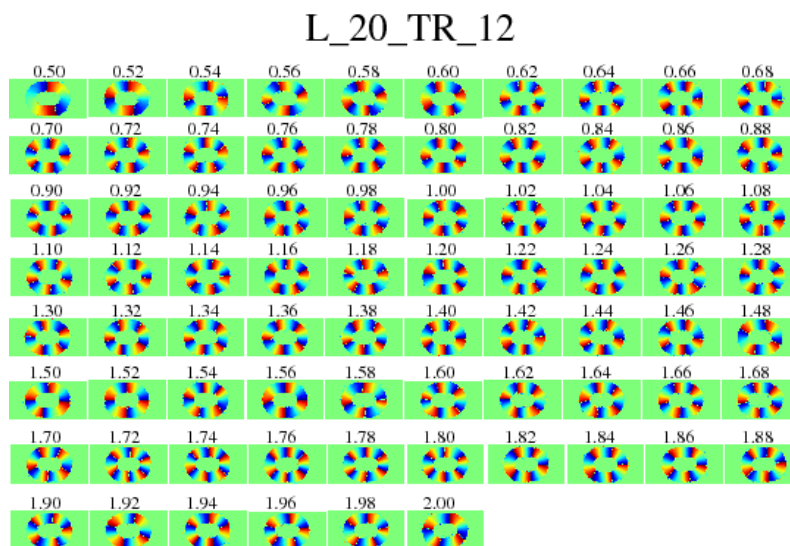


Figure 3.23: L_20_TR_12

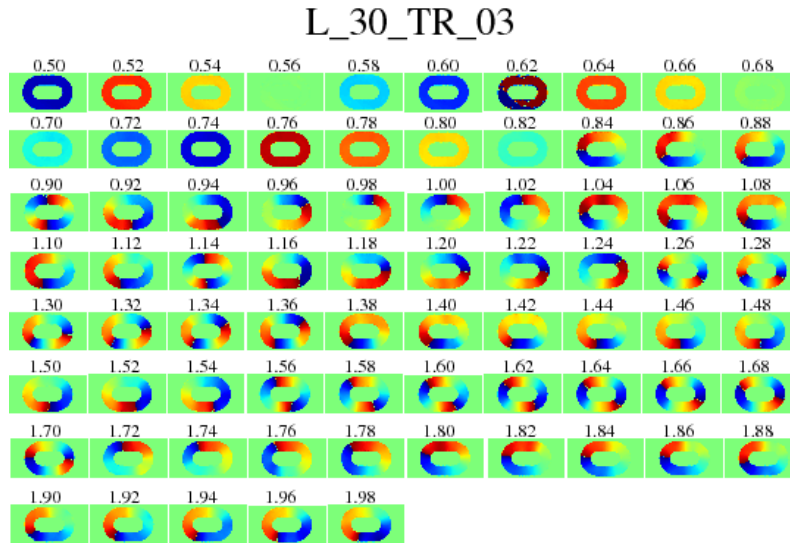


Figure 3.24: L_30_TR_03

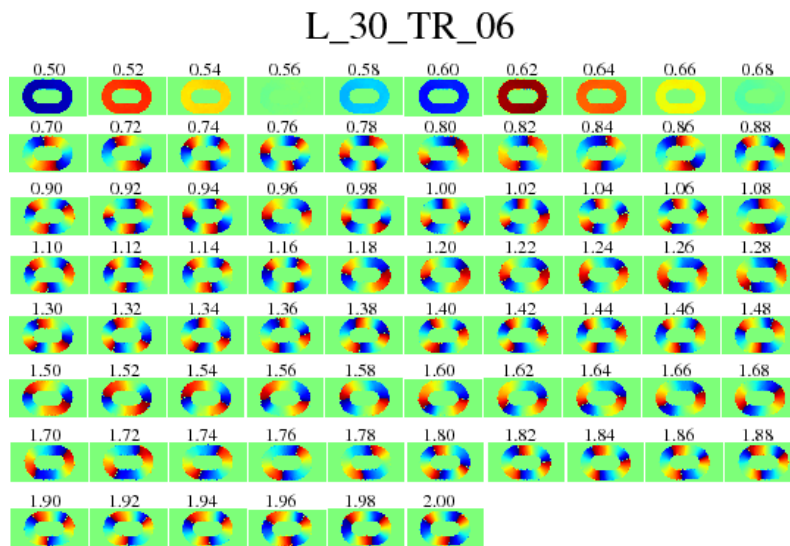


Figure 3.25: L_30_TR_06

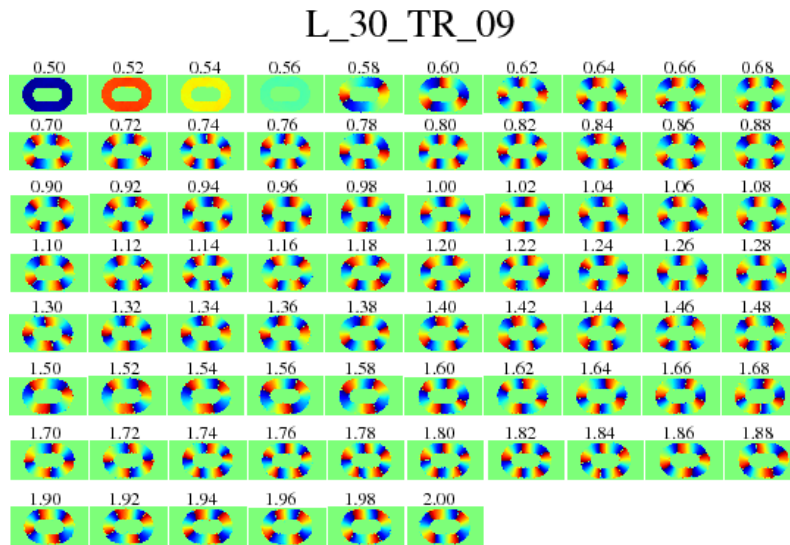


Figure 3.26: L_30_TR_09

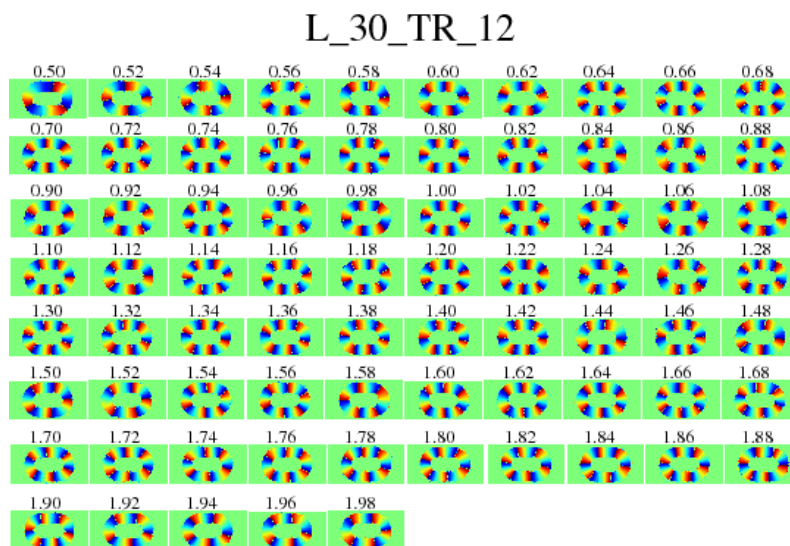


Figure 3.27: L_30_TR_12

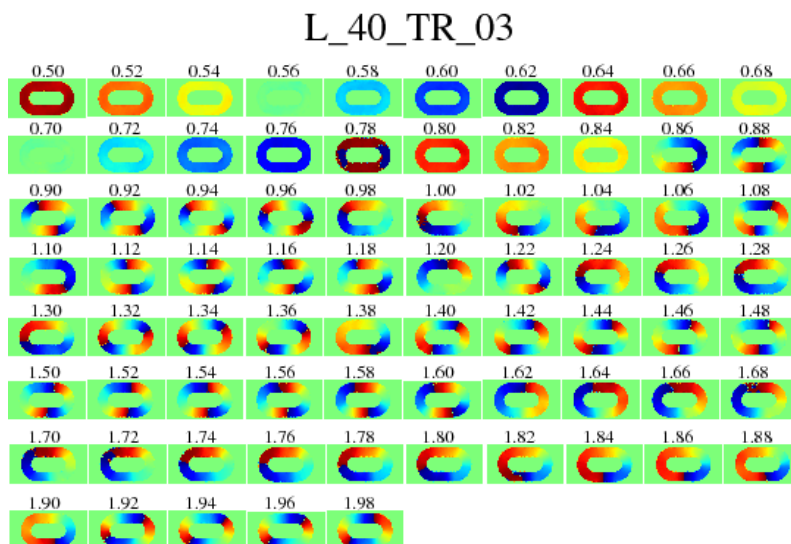


Figure 3.28: L_40_TR_03

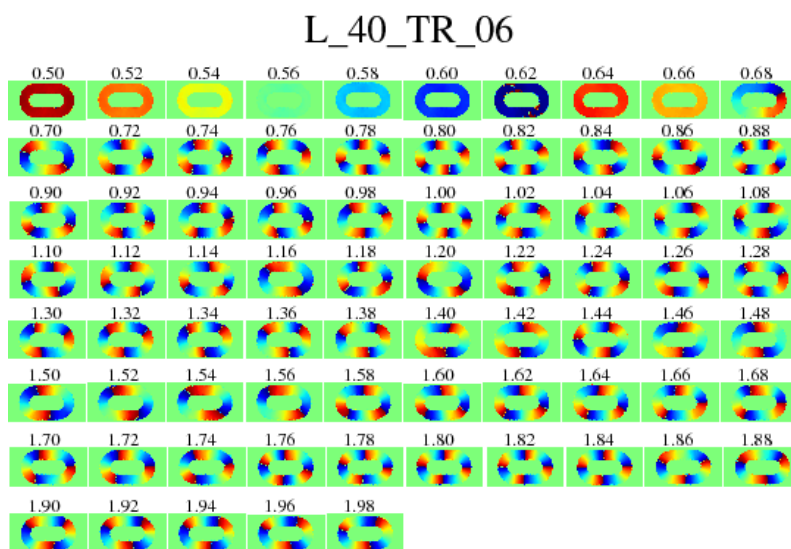


Figure 3.29: L_40_TR_06

L_40_TR_09

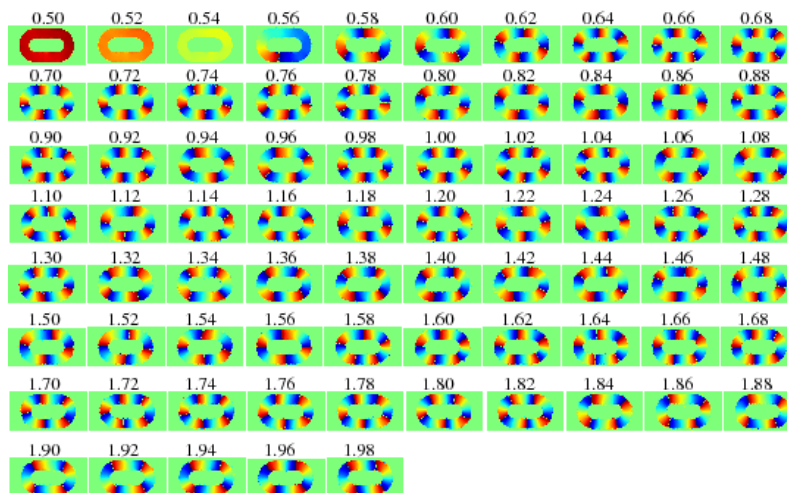


Figure 3.30: L_40_TR_09

L_40_TR_12

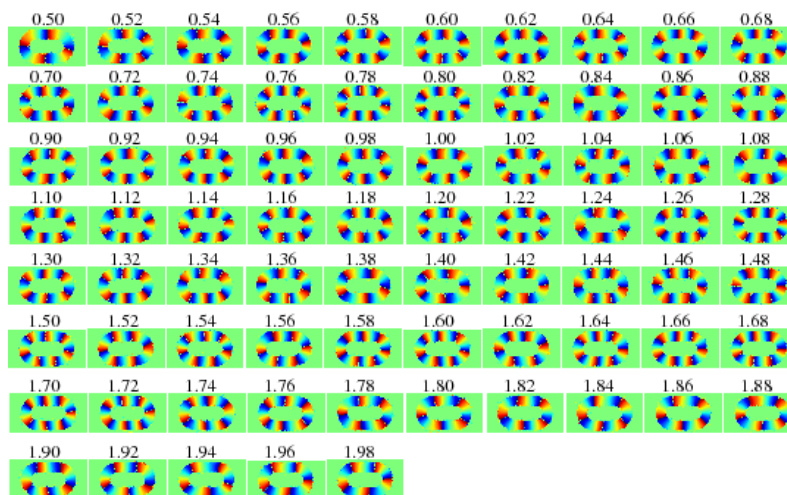


Figure 3.31: L_40_TR_12

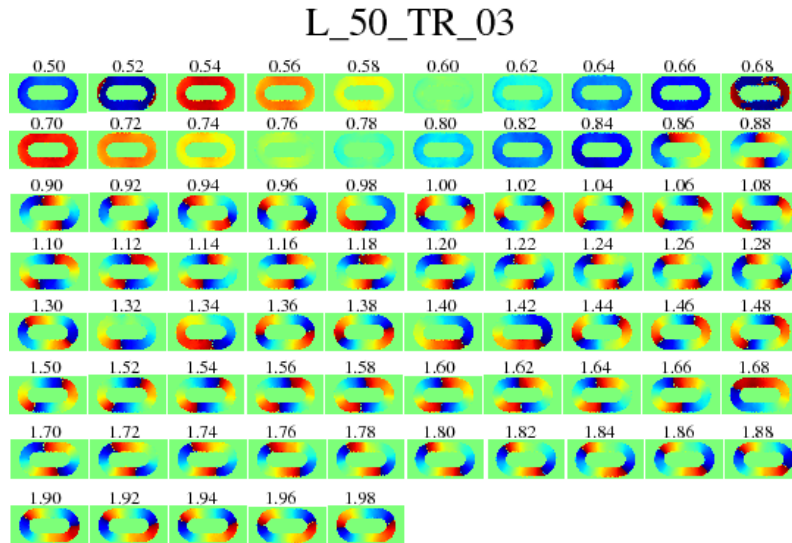


Figure 3.32: L_50_TR_03

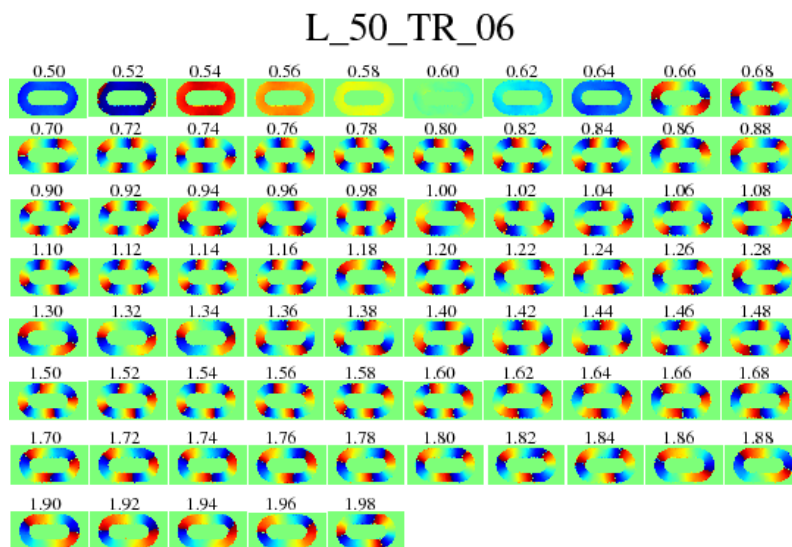


Figure 3.33: L_50_TR_06

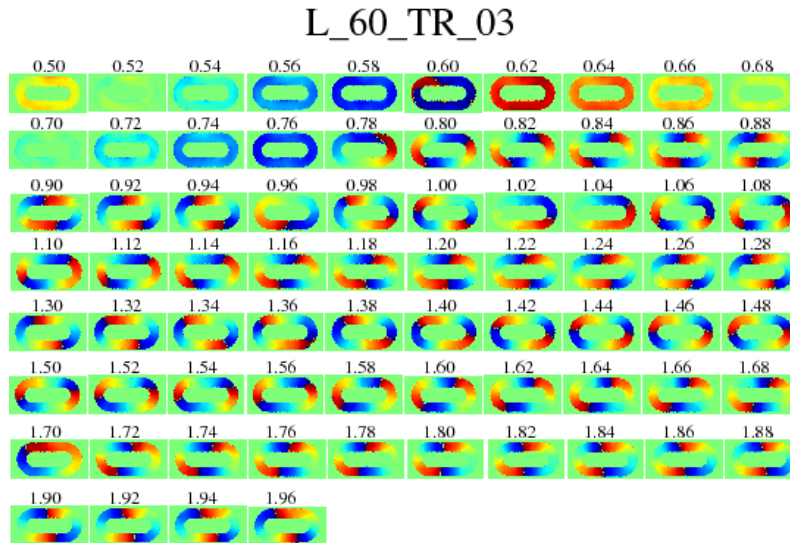


Figure 3.36: L_60_TR_03

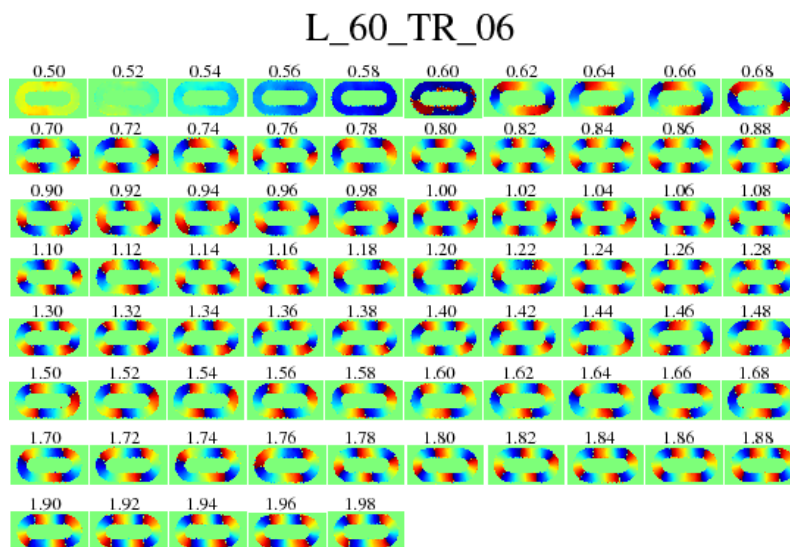


Figure 3.37: L_60_TR_06

L_60_TR_09

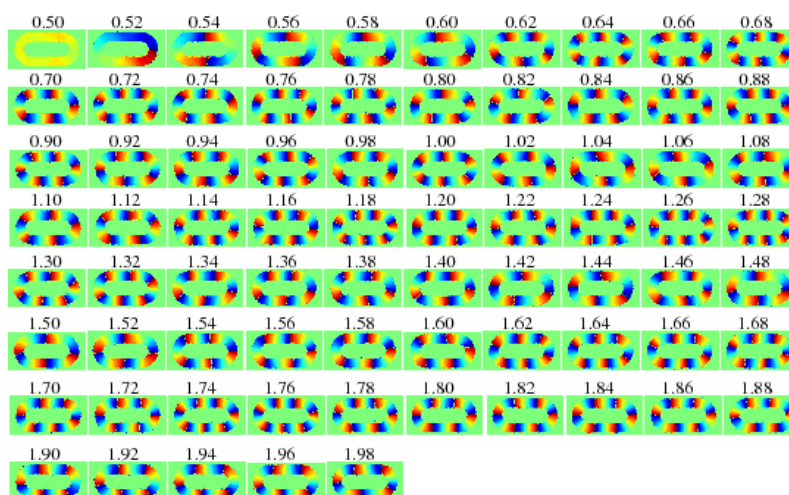


Figure 3.38: L_60_TR_09

L_60_TR_12

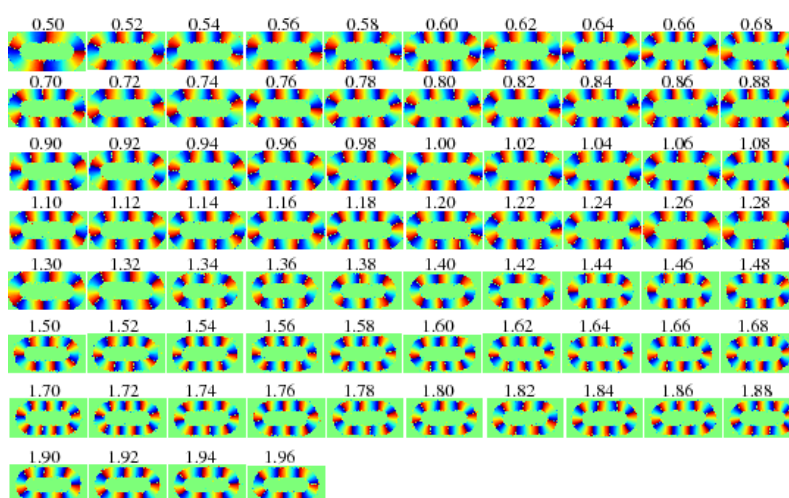


Figure 3.39: L_60_TR_12

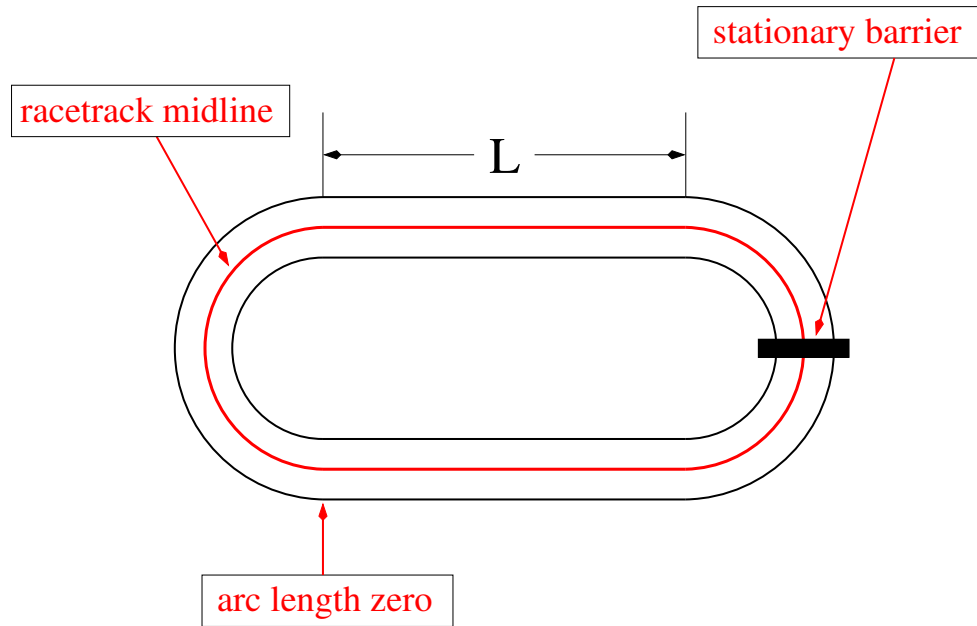


Figure 3.40: Midline, shown in red, of the racetrack showing where the data from the 3D GPE was extracted.

3.6 Condensate behavior along the racetrack midline

We mined data from a given 3D GPE simulation by extracting the condensate wave function values along the midtrack of the racetrack as a function of time. This line is shown in red in Fig. 3.40. We also plotted this data in the reference frame in which the barrier is at rest. The wave function 1D coordinate system is referenced to the arc length distance as measured going counterclockwise from the left end of the bottom straightaway. This starting point is also shown in the figure.

Figure 3.41 shows an example of data mined from the simulation where $L = 30\mu\text{m}$, $\text{TR} = 09$, and $V_{p,\text{max}} = 544.7E_0$ (scaled units) which is $V_{p,\text{max}} \approx 54\text{ nK}$. The six

plots show, at six different times, the condensate density (red) and phase (green) along the racetrack midline and represented in the reference frame in which the barrier is at rest. The left vertical axis shows the value of the density (in arbitrary units) while the right vertical axis shows the value of the phase and is measured in units of 2π .

As time progresses, the density develops a dip at the site of the barrier as the barrier height increases. The density dip eventually reaches the bottom, stays on for a while, and then disappears. The density stays approximately constant for the rest of the evolution after the stirring is over. The phase jumps around while the stirring is going on but we observed that, by the time the barrier starts to ramp off, the final value of the phase has been set. In the future we hope to develop a 1D model of this process that will match the behavior mined from the 3D GPE simulations.

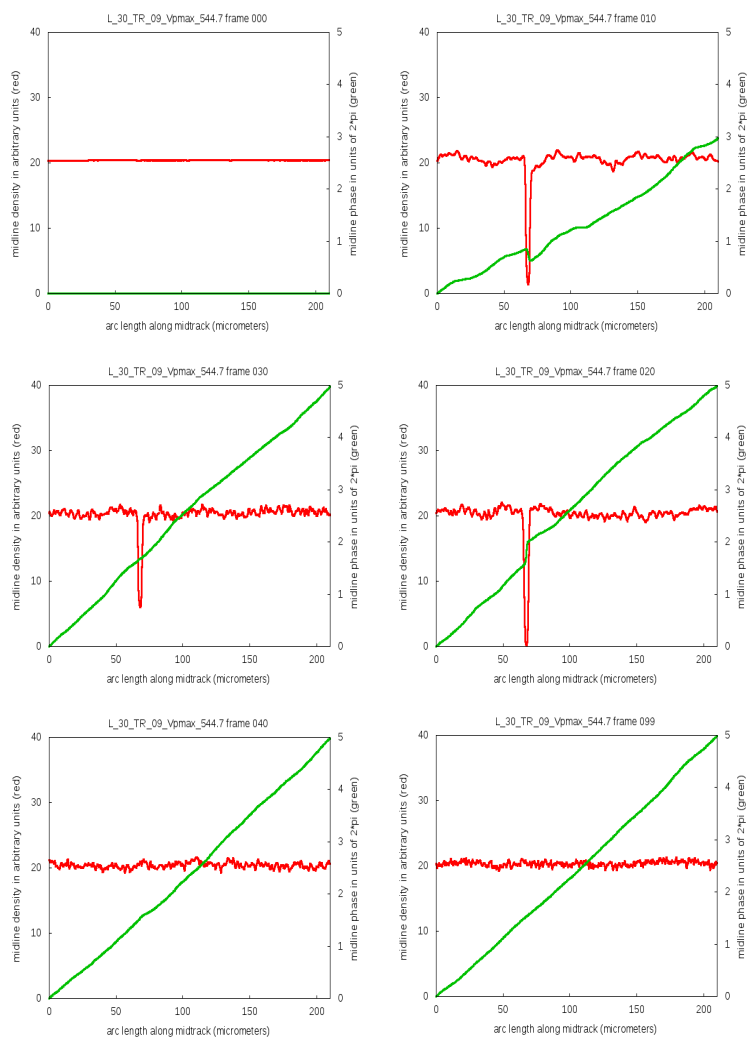


Figure 3.41: Plots of the BEC density (red) and the phase (green) at points along the midline in the barrier rest frame. See text for details.

CHAPTER 4

SUMMARY

In this thesis we studied theoretically whether and how smooth flow can be produced by stirring a racetrack atom circuit containing a Bose–Einstein condensate. Smooth flow is essential if atom circuits are to be useful for applications such as quantum simulators, quantum sensors, and as elements in integrated circuits. Thus whether smooth flow can be produced in such circuits is an interesting and topical question.

In our study we tried stirring the racetrack condensate with two kinds of stirrers. These were (1) a rotating elliptical barrier inspired by the idea of a peristaltic pump and (2) a rectangular barrier moving along and oriented perpendicular to the racetrack midline and twice as wide as the racetrack width. We were not able to produce smooth flow using the elliptical barrier because all of our simulations contained significant amounts of turbulence. While turbulence is an interesting subject in its own right and may be important to understand in the context of atom circuits, the study of turbulence was not our goal here.

On the other hand we were able to produce smooth flow by stirring with a rectangular barrier. We found that this type of barrier was quite effective in producing flow under a variety of conditions. This result is of some importance to the field of atomtronics because of the essential nature of flow in atom–circuit operations.

Given the fact that the rectangular barrier can easily produce smooth flow in the racetrack atom circuit, we decided to conduct a systematic study of how much flow

will be produced by stirring for different racetrack geometries, stirring speeds, and barrier strengths. This study was carried out by performing over 2000 simulations each for a different set of these three quantities.

The results of this study revealed several interesting features regarding the amount of flow produced by stirring. These features were the following

- Stirring a racetrack condensate with a rectangular barrier does produce smooth flow
- The amount of flow produced by stirring, at fixed L and TR , is not a monotonic function of the barrier strength V_{pmax} . We observed oscillations in the flow produced as V_{pmax} increases.
- The amount of flow produced by stirring, for fixed L and TR , can jump by more than one as V_{pmax} increases.
- For weak barriers no flow is produced but, when the barrier is finally strong enough to produce non-zero flow, the amount produced isn't always one unit of flow.

Based on these phenomena, we decided that developing a simple 1D model that could easily predict the flow produced by stirring under a given set of conditions.

We have been unable to devise such a model as yet. However, we were able to mine data from the 3D GPE simulations in order to gain a better understanding of condensate behavior and to test any 1D model that we develop.

REFERENCES

- [1] S. Eckel, J. Lobb, M. Edwards, W. Phillips, J. Lee, F. Jendrzejewski, N. Murray, and G. Campbell, *Quantized hysteresis in a superfluid BEC atomtronic circuit*, Nature **506**, 200 (2014).
- [2] L. Amico, G. Birkl, M. Boshier, and L.-C. Kwek, *Focus on atomtronics-enabled quantum technologies*, New Journal of Physics **19**, 020201 (2017).
- [3] Y. S. Greenberg, *Application of superconducting quantum interference devices to nuclear magnetic resonance*, Rev. Mod. Phys. **70**, 175 (1998).
- [4] D. Aghamalyan, M. Cominotti, M. Rizzi, D. Rossini, F. Hekking, A. Minguzzi, L.-C. Kwek, and L. Amico, *Coherent superposition of current flows in an atomtronic quantum interference device*, New Journal of Physics **17**, 045023 (2015).
- [5] J. R. M. de Nova, F. Sols, and I. Zapata, *Entanglement and violation of classical inequalities in the Hawking radiation of flowing atom condensates*, New Journal of Physics **17**, 105003 (2015).
- [6] N. Barberán, D. Dagnino, M. A. García-March, A. Trombettoni, J. Taron, and M. Lewenstein, *Quantum simulation of conductivity plateaux and fractional quantum Hall effect using ultracold atoms*, New Journal of Physics **17**, 125009 (2015).
- [7] A. Quelle, M. O. Goerbig, and C. M. Smith, *Bandwidth-resonant Floquet states in honeycomb optical lattices*, New Journal of Physics **18**, 015006 (2016).
- [8] G. Arwas and D. Cohen, *Chaos and two-level dynamics of the atomtronic quantum interference device*, New Journal of Physics **18**, 015007 (2016).
- [9] E. O. Karabulut, F. Malet, A. L. Fetter, G. M. Kavoulakis, and S. M. Reimann, *Spin-orbit-coupled Bose-Einstein-condensed atoms confined in annular potentials*, New Journal of Physics **18**, 015013 (2016).
- [10] A. Safavi-Naini, B. Capogrosso-Sansone, A. Kuklov, and V. Penna, *Quasi-molecular bosonic complexes-a pathway to SQUID with controlled sensitivity*, New Journal of Physics **18**, 025017 (2016).

- [11] A. Gallemí, M. Guilleumas, J. Martorell, R. Mayol, A. Polls, and B. Juliá-Díaz, *Robustness of discrete semifluxons in closed Bose–Hubbard chains*, New Journal of Physics **18**, 075005 (2016).
- [12] F. Buccheri, G. D. Bruce, A. Trombettoni, D. Cassettari, H. Babujian, V. E. Korepin, and P. Sodano, *Holographic optical traps for atom-based topological Kondo devices*, New Journal of Physics **18**, 075012 (2016).
- [13] S. Butera, M. Valiente, and P. Öhberg, *Vortex dynamics in superfluids governed by an interacting gauge theory*, New Journal of Physics **18**, 085001 (2016).
- [14] A. Gallemí, A. M. Mateo, R. Mayol, and M. Guilleumas, *Coherent quantum phase slip in two-component bosonic atomtronic circuits*, New Journal of Physics **18**, 015003 (2016).
- [15] A. Kumar, N. Anderson, W. D. Phillips, S. Eckel, G. K. Campbell, and S. Stringari, *Minimally destructive, Doppler measurement of a quantized flow in a ring-shaped Bose–Einstein condensate*, New Journal of Physics **18**, 025001 (2016).
- [16] D. Gallucci and N. P. Proukakis, *Engineering dark solitary waves in ring-trap Bose–Einstein condensates*, New Journal of Physics **18**, 025004 (2016).
- [17] V. A. Henderson, P. F. Griffin, E. Riis, and A. S. Arnold, *Comparative simulations of Fresnel holography methods for atomic waveguides*, New Journal of Physics **18**, 025007 (2016).
- [18] T. A. Bell, J. A. P. Glidden, L. Humbert, M. W. J. Bromley, S. A. Haine, M. J. Davis, T. W. Neely, M. A. Baker, and H. Rubinsztein-Dunlop, *Bose–Einstein condensation in large time-averaged optical ring potentials*, New Journal of Physics **18**, 035003 (2016).
- [19] G. A. Sinuco-León and B. M. Garraway, *Addressed qubit manipulation in radio-frequency dressed lattices*, New Journal of Physics **18**, 035009 (2016).
- [20] D. Aghamalyan, N. T. Nguyen, F. Auksztol, K. S. Gan, M. M. Valado, P. C. Condylis, L.-C. Kwek, R. Dumke, and L. Amico, *An atomtronic flux qubit: a ring lattice of Bose–Einstein condensates interrupted by three weak links*, New Journal of Physics **18**, 075013 (2016).

- [21] P. Navez, S. Pandey, H. Mas, K. Poullos, T. Fernholz, and W. von Klitzing, *Matter-wave interferometers using TAAP rings*, New Journal of Physics **18**, 075014 (2016).
- [22] C. Ryu and M. G. Boshier, *Integrated coherent matter wave circuits*, New Journal of Physics **17**, 092002 (2015).
- [23] Z. Zhang, V. Dunjko, and M. Olshanii, *Atom transistor from the point of view of nonequilibrium dynamics*, New Journal of Physics **17**, 125008 (2015).
- [24] Y.-H. Wang, A. Kumar, F. Jendrzejewski, R. M. Wilson, M. Edwards, S. Eckel, G. K. Campbell, and C. W. Clark, *Resonant wavepackets and shock waves in an atomtronic SQUID*, New Journal of Physics **17**, 125012 (2015).
- [25] A. M. Mateo and J. Brand, *Stability and dispersion relations of three-dimensional solitary waves in trapped Bose–Einstein condensates*, New Journal of Physics **17**, 125013 (2015).
- [26] J. Polo, A. Benseny, T. Busch, V. Ahufinger, and J. Mompart, *Transport of ultracold atoms between concentric traps via spatial adiabatic passage*, New Journal of Physics **18**, 015010 (2016).
- [27] S. C. Caliga, C. J. E. Straatsma, A. A. Zozulya, and D. Z. Anderson, *Principles of an atomtronic transistor*, New Journal of Physics **18**, 015012 (2016).
- [28] S. C. Caliga, C. J. E. Straatsma, and D. Z. Anderson, *Transport dynamics of ultracold atoms in a triple-well transistor-like potential*, New Journal of Physics **18**, 025010 (2016).
- [29] M. W. Gempel, T. Hartmann, T. A. Schulze, K. K. Voges, A. Zenesini, and S. Ospelkaus, *Versatile electric fields for the manipulation of ultracold NaK molecules*, New Journal of Physics **18**, 045017 (2016).
- [30] Y. Japha, S. Zhou, M. Keil, R. Folman, C. Henkel, and A. Vardi, *Suppression and enhancement of decoherence in an atomic Josephson junction*, New Journal of Physics **18**, 055008 (2016).
- [31] M. Pasienski and B. DeMarco, *A high-accuracy algorithm for designing arbitrary holographic atom traps*, Optical Express **16**, 2176 (2008).

- [32] A. Gaunt and Z. Hadzibabic, *Robust digital holography For ultracold atom trapping*, Scientific Reports **2**, 721 (2008).
- [33] K. Henderson, C. Ryu, C. MacCormick, and M. Boshier, *Experimental demonstration of painting arbitrary and dynamic potentials for Bose–Einstein condensates*, New Journal of Physics **11**, 043030 (2009).
- [34] J. Lee, B. Mcilvain, C. Lobb, and W. Hill, *Analogs of Basic Electronic Circuit Elements in a Free-Space Atom Chip*, Scientific Reports **3**, 1034 (2012).
- [35] A. Ramanathan, K. Wright, S. Muniz, M. Zelan, W. Hill, C. Lobb, K. Helmerson, W. Phillips, and G. Campbell, *Superflow in a toroidal Bose-Einstein condensate: an atom circuit with a tunable weak link*, Physical Review Letters **106**, 130401 (2011).
- [36] K. Wright, R. Blakestad, C. Lobb, W. Phillips, and G. Campbell, *Driving phase slips in a superfluid atom circuit with a rotating weak link*, Physical Review Letters **110**, 025302 (2013).
- [37] C. Ryu, P. W. Blackburn, A. A. Blinova, and M. G. Boshier, *Experimental Realization of Josephson Junctions for an Atom SQUID*, Phys. Rev. Lett. **111**, 205301 (2013).
- [38] C. Ryu, K. C. Henderson, and M. G. Boshier, *Creation of matter wave Bessel beams and observation of quantized circulation in a Bose–Einstein condensate*, New Journal of Physics **16**, 013046 (2014).
- [39] B. T. Seaman, M. Krämer, D. Z. Anderson, and M. J. Holland, *Atomtronics: Ultracold-atom analogs of electronic devices*, Phys. Rev. A **75**, 023615 (2007).
- [40] G. Gauthier, I. Lenton, N. M. Parry, M. Baker, M. J. Davis, H. Rubinsztein-Dunlop, and T. W. Neely, *Direct imaging of a digital-micromirror device for configurable microscopic optical potentials*, Optica **3**, 1136 (2016).
- [41] M. Gajdacz, A. J. Hilliard, M. A. Kristensen, P. L. Pedersen, C. Klempt, J. J. Arlt, and J. F. Sherson, *Preparation of Ultracold Atom Clouds at the Shot Noise Level*, Phys. Rev. Lett. **117**, 073604 (2016).
- [42] A. Messiah, *Quantum Mechanics*, Dover Publications, 2014.
- [43] C. J. Pethick and H. Smith, *Bose–Einstein Condensation in Dilute Gases*, Cambridge University Press, 2nd edition, 2008.

- [44] M. H. Anderson, J. R. Ensher, M. R. Matthews, C. E. Wieman, and E. A. Cornell, *Observation of Bose-Einstein condensation in a dilute atomic vapor*, *Science* **269**, 198 (1995).
- [45] L. Pitaevskii and S. Stringari, *Bose–Einstein Condensation and Superfluidity*, Oxford University Press, 2016.
- [46] E. Lundh, C. J. Pethick, and H. Smith, *Zero-temperature properties of a trapped Bose-condensed gas: Beyond the Thomas-Fermi approximation*, *Phys. Rev. A* **55**, 2126 (1997).
- [47] P. A. Ruprecht, M. J. Holland, K. Burnett, and M. Edwards, *Time-dependent solution of the nonlinear Schrödinger equation for Bose-condensed trapped neutral atoms*, *Phys. Rev. A* **51**, 4704 (1995).
- [48] C. C. Bradley, C. A. Sackett, J. J. Tollett, and R. G. Hulet, *Evidence of Bose-Einstein Condensation in an Atomic Gas with Attractive Interactions*, *Phys. Rev. Lett.* **75**, 1687 (1995).
- [49] C. Cohen-Tannoudji and D. Guéry-Odelin, *Advances in Atomic Physics: An Overview*, World Scientific, 2011.
- [50] P. Muruganandam and S. Adhikari, *Fortran programs for the time-dependent Gross–Pitaevskii equation in a fully anisotropic trap*, *Computer Physics Communications* **180**, 1888 (2009).
- [51] N. Murray, M. Krygier, M. Edwards, K. C. Wright, G. K. Campbell, and C. W. Clark, *Probing the circulation of ring-shaped Bose-Einstein condensates*, *Phys. Rev. A* **88**, 053615 (2013).

Appendix A

THE GROUND-STATE ENERGY FUNCTIONAL

In this appendix we provide the details of the calculation of the expression for the ground-state energy when the many-body wave function is assumed to be the N -fold product of the same single-particle condensate wave function. The variational approximation method determines the defining equation for the unknown condensate wave function by minimizing the ground-state energy functional

$$E[\phi^*] \equiv \langle \Psi_{\text{MB}} | H_{\text{MB}} | \Psi_{\text{MB}} \rangle \quad (\text{A.1})$$

subject to the constraint that $\phi(\mathbf{r})$ be normalized to unity. In integral form this is

$$E[\phi^*] = \int d^3 r_1 \dots \int d^3 r_N \Psi_{\text{MB}}^* H_{\text{MB}} \Psi_{\text{MB}} \quad (\text{A.2})$$

$$\begin{aligned} E[\phi^*] &= \int d^3 r_1 \dots \int d^3 r_N \phi^*(\mathbf{r}_1) \dots \phi^*(\mathbf{r}_N) \\ &\times \left(\sum_{i=1}^N \left(-\frac{\hbar^2}{2M} \nabla_i^2 + V(\mathbf{r}_i) \right) + g \sum_{j=2}^N \sum_{i=j}^{j-2} \delta(\mathbf{r}_i - \mathbf{r}_j) \right) \phi(\mathbf{r}_1) \dots \phi(\mathbf{r}_N) \end{aligned} \quad (\text{A.3})$$

$$\begin{aligned} E[\phi^*] &= \int d^3 r_1 \dots \int d^3 r_N \phi^*(\mathbf{r}_1) \dots \phi^*(\mathbf{r}_N) \\ &\sum_{i=1}^N \left(-\frac{\hbar^2}{2M} \nabla_i^2 + V(\mathbf{r}_i) \right) \phi(\mathbf{r}_1) \dots \phi(\mathbf{r}_N) + \\ &\int d^3 r_1 \dots \int d^3 r_N \phi^*(\mathbf{r}_1) \dots \phi^*(\mathbf{r}_N) \left(g \sum_{j=2}^N \sum_{i=j}^{j-2} \delta(\mathbf{r}_i - \mathbf{r}_j) \right) \phi(\mathbf{r}_1) \dots \phi(\mathbf{r}_N) \end{aligned} \quad (\text{A.4})$$

$$\begin{aligned}
E[\phi^*] &= \int d^3r_1 |\phi(\mathbf{r}_1)|^2 \int d^3r_2 |\phi(\mathbf{r}_2)|^2 \dots \int d^3r_{i-1} |\phi(\mathbf{r}_{i-1})|^2 \\
&\int d^3r_i \phi^*(\mathbf{r}_i) \left(-\frac{\hbar^2}{2M} \nabla_i^2 + V(\mathbf{r}_i) \right) \phi(\mathbf{r}_i) \dots \int d^3r_N |\phi(\mathbf{r}_N)|^2 + \\
&g \sum_{j=2}^N \sum_{i=j}^{j-2} \int d^3r_i \int d^3r_j \phi^*(\mathbf{r}_i) \phi^*(\mathbf{r}_j) \delta(\mathbf{r}_i - \mathbf{r}_j) \phi(\mathbf{r}_i) \phi(\mathbf{r}_j)
\end{aligned} \tag{A.5}$$

So, using the relation

$$\int_a^b F(x) \delta(x - x_0) dx = \begin{cases} f(x_0) & a < x < b \\ 0 & \text{otherwise} \end{cases} \tag{A.6}$$

and also since bosonic atoms have the same single-particle state, hence

$$\begin{aligned}
E[\phi] &= N \int d^3r \phi^*(\mathbf{r}) \left(-\frac{\hbar^2}{2M} \nabla^2 + V(\mathbf{r}) \right) \phi(\mathbf{r}) + \\
&\frac{N(N-1)}{2} g \int d^3r \phi^*(\mathbf{r}) \phi^*(\mathbf{r}) \phi(\mathbf{r}) \phi(\mathbf{r})
\end{aligned} \tag{A.7}$$

$$E[\phi] = N \int d^3r \phi^*(\mathbf{r}) \left(-\frac{\hbar^2}{2M} \nabla^2 + V(\mathbf{r}) \right) \phi(\mathbf{r}) + \frac{N(N-1)}{2} g \int d^3r |\phi(\mathbf{r})|^4 \tag{A.8}$$

so $N \frac{N-1}{2}$ is the number of terms in the interaction energy, that is the number of ways of making pairs of bosons. Considering the uniform Bose gas. In a uniform system of volume V , the wave function of a particle in the ground state is $\frac{1}{V^{1/2}}$ and therefore the interaction energy of a pair of particles is $\frac{g}{V}$. The energy of a state with N boson all in the same state is this quantity multiplied by the number of possible ways of making pairs of bosons, $\frac{N(N-1)}{2}$.

In this approximation, the energy is

$$E = \frac{N(N-1)}{2V} g \cong \frac{1}{2} V n^2 g \tag{A.9}$$

where $n = \frac{N}{V}$, we assumed that $N \gg 1$ By introducing the concept of the wave function $\Psi(r)$ of the condensed state by the definition

$$\psi(\mathbf{r}) = N^{1/2} \phi(\mathbf{r}) \tag{A.10}$$

The condensate density is given by $n(r) = |\psi(r)|^2$ and with the neglect of terms of order $\frac{1}{N}$, the energy of the system becomes

$$E[\psi] = N \left[\int d^3r \left(-\frac{\hbar^2}{2M} |\nabla N^{-\frac{1}{2}} \psi(\mathbf{r})|^2 + V(\mathbf{r}) |N^{-\frac{1}{2}} \psi(\mathbf{r})|^2 + \frac{N}{2} g |N^{-\frac{1}{2}} \psi(\mathbf{r})|^4 \right) \right] \quad (\text{A.11})$$

so

$$E[\psi] = \int d^3r \left(-\frac{\hbar^2}{2M} |\nabla \psi(\mathbf{r})|^2 + V(\mathbf{r}) |\psi(\mathbf{r})|^2 + \frac{1}{2} g |\psi(\mathbf{r})|^4 \right) \quad (\text{A.12})$$

Appendix B

CONDENSATE VELOCITY DISTRIBUTION

In this appendix expressions are derived for the condensate velocity distribution as determined from the wave function referenced to the laboratory frame and also with respect to a reference rotating about the z axis. In our study of stirred atom circuits, the z axis is perpendicular to the horizontal plane in which the condensate is strongly confined.

B.1 Lab frame velocity distribution

The lab-frame condensate velocity distribution is the gradient of the phase of the condensate wave function. We start with the time-dependent GPE which, in the lab frame, has the form

$$i\hbar \frac{\partial \Psi(\mathbf{r}, t)}{\partial t} = -\frac{\hbar^2}{2M} \nabla^2 \Psi(\mathbf{r}, t) + V(\mathbf{r}, t) \Psi(\mathbf{r}, t) + gN |\Psi(\mathbf{r}, t)|^2 \Psi(\mathbf{r}, t) \quad (\text{B.1})$$

We let $\rho(\mathbf{r}, t) \equiv \Psi^*(\mathbf{r}, t) \Psi(\mathbf{r}, t)$ which is the probability density. Differentiating ρ with respect to t gives

$$\frac{\partial \rho}{\partial t} = \frac{\partial \Psi^*}{\partial t} \Psi + \Psi^* \frac{\partial \Psi}{\partial t} \quad (\text{B.2})$$

The complex conjugate of equation (B.1) is

$$-i\hbar \frac{\partial \Psi^*(\mathbf{r}, t)}{\partial t} = -\frac{\hbar^2}{2M} \nabla^2 \Psi^*(\mathbf{r}, t) + V(\mathbf{r}) \Psi^*(\mathbf{r}, t) + gN |\Psi(\mathbf{r}, t)|^2 \Psi^*(\mathbf{r}, t) \quad (\text{B.3})$$

if we multiply Eq. (B.1) by $\Psi^*(\mathbf{r}, t)$ and equation (B.3) by $\Psi(\mathbf{r}, t)$ we have

$$i\hbar \Psi^* \frac{\partial \Psi}{\partial t} = -\frac{\hbar^2}{2M} \Psi^* \nabla^2 \Psi + \Psi^* V(\mathbf{r}) \Psi + gN |\Psi|^2 \Psi^* \Psi \quad (\text{B.4})$$

$$-i\hbar\Psi\frac{\partial\Psi^*}{\partial t} = -\frac{\hbar^2}{2M}\Psi\nabla^2\Psi^* + \Psi V(\mathbf{r})\Psi^* + gN|\Psi|^2\Psi^*\Psi \quad (\text{B.5})$$

Subtracts the two equations, one arrives at the equation

$$i\hbar\left(\frac{\partial\Psi^*}{\partial t}\Psi + \Psi^*\frac{\partial\Psi}{\partial t}\right) = -\frac{\hbar^2}{2M}\Psi^*\nabla^2\Psi + \frac{\hbar^2}{2M}\Psi\nabla^2\Psi^* \quad (\text{B.6})$$

$$\left(\frac{\partial\Psi^*}{\partial t}\Psi + \Psi^*\frac{\partial\Psi}{\partial t}\right) = -\frac{\hbar}{2Mi}\left(\Psi^*\nabla^2\Psi - \Psi\nabla^2\Psi^*\right) \quad (\text{B.7})$$

from equation (B.2), equation (B.7) becomes

$$\frac{\partial\rho}{\partial t} = -\frac{\hbar}{2Mi}\left(\Psi^*\nabla^2\Psi - \Psi\nabla^2\Psi^*\right) \quad (\text{B.8})$$

$$\frac{\partial\rho}{\partial t} = -\frac{\hbar}{2Mi}\left[\Psi^*\left(\frac{\partial^2\Psi}{\partial x^2} + \frac{\partial^2\Psi}{\partial y^2} + \frac{\partial^2\Psi}{\partial z^2}\right) - \Psi\left(\frac{\partial^2\Psi^*}{\partial x^2} + \frac{\partial^2\Psi^*}{\partial y^2} + \frac{\partial^2\Psi^*}{\partial z^2}\right)\right] \quad (\text{B.9})$$

$$\frac{\partial\rho}{\partial t} = -\frac{\hbar}{2Mi}\left[\Psi^*\frac{\partial^2\Psi}{\partial x^2} + \Psi^*\frac{\partial^2\Psi}{\partial y^2} + \Psi^*\frac{\partial^2\Psi}{\partial z^2} - \Psi\frac{\partial^2\Psi^*}{\partial x^2} - \Psi\frac{\partial^2\Psi^*}{\partial y^2} - \Psi\frac{\partial^2\Psi^*}{\partial z^2}\right] \quad (\text{B.10})$$

$$\frac{\partial\rho}{\partial t} = -\frac{\hbar}{2Mi}\left[\Psi^*\frac{\partial^2\Psi}{\partial x^2} - \Psi\frac{\partial^2\Psi^*}{\partial x^2} + \Psi^*\frac{\partial^2\Psi}{\partial y^2} - \Psi\frac{\partial^2\Psi^*}{\partial y^2} + \Psi^*\frac{\partial^2\Psi}{\partial z^2} - \Psi\frac{\partial^2\Psi^*}{\partial z^2}\right] \quad (\text{B.11})$$

$$\begin{aligned} \frac{\partial\rho}{\partial t} = \frac{\partial\rho}{\partial t} & \left[\frac{\partial}{\partial x} \left(\Psi^* \frac{\partial\Psi}{\partial x} - \Psi \frac{\partial\Psi^*}{\partial x} \right) + \right. \\ & \frac{\partial}{\partial y} \left(\Psi^* \frac{\partial\Psi}{\partial y} - \Psi \frac{\partial\Psi^*}{\partial y} \right) + \\ & \left. \frac{\partial}{\partial z} \left(\Psi^* \frac{\partial\Psi}{\partial z} - \Psi \frac{\partial\Psi^*}{\partial z} \right) \right] \end{aligned} \quad (\text{B.12})$$

Since

$$\nabla = i\frac{\partial}{\partial x} + j\frac{\partial}{\partial y} + k\frac{\partial}{\partial z} \quad (\text{B.13})$$

So

$$\begin{aligned} \nabla \cdot \left(\Psi^* \nabla \Psi - \Psi \nabla \Psi^* \right) &= \frac{\partial}{\partial x} \left(\Psi^* \frac{\partial \Psi}{\partial x} - \Psi \frac{\partial \Psi^*}{\partial x} \right) \\ &+ \frac{\partial}{\partial y} \left(\Psi^* \frac{\partial \Psi}{\partial y} - \Psi \frac{\partial \Psi^*}{\partial y} \right) \\ &+ \frac{\partial}{\partial z} \left(\Psi^* \frac{\partial \Psi}{\partial z} - \Psi \frac{\partial \Psi^*}{\partial z} \right) \end{aligned} \quad (\text{B.14})$$

hence

$$\frac{\partial \rho}{\partial t} = -\frac{\hbar}{2Mi} \left[\nabla \cdot \left(\Psi^* \nabla \Psi - \Psi \nabla \Psi^* \right) \right] \quad (\text{B.15})$$

$$\frac{\partial \rho}{\partial t} = -\nabla \cdot \frac{\hbar}{2Mi} \left(\Psi^* \nabla \Psi - \Psi \nabla \Psi^* \right) \quad (\text{B.16})$$

So, define the probability current as

$$\mathbf{J} = \frac{\hbar}{2Mi} \left(\Psi^* \nabla \Psi - \Psi \nabla \Psi^* \right) \quad (\text{B.17})$$

Hence equation (B.16) becomes

$$\frac{\partial \rho}{\partial t} + \nabla \cdot \mathbf{J} = 0 \quad (\text{B.18})$$

Which is equal to the equation of continuity. Now let $\mathbf{J} = \rho \mathbf{v}$. Where \mathbf{v} is the velocity distribution. So, since $\mathbf{v} = \mathbf{J}/\rho$ we have

$$\mathbf{v}(\mathbf{r}, t) = \frac{\hbar}{2Mi} \left(\frac{\Psi^*(\mathbf{r}, t) \nabla \Psi(\mathbf{r}, t) - \Psi(\mathbf{r}, t) \nabla \Psi^*(\mathbf{r}, t)}{\Psi^*(\mathbf{r}, t) \Psi(\mathbf{r}, t)} \right) \quad (\text{B.19})$$

If we write $\Psi(\mathbf{r})$ in term of its amplitude f and phase ϕ

$$\Psi(\mathbf{r}, t) = f(\mathbf{r}, t) e^{i\phi(\mathbf{r}, t)} \quad (\text{B.20})$$

complex conjugate is,

$$\Psi^*(\mathbf{r}, t) = f(\mathbf{r}, t)e^{-i\phi(\mathbf{r}, t)} \quad (\text{B.21})$$

So, equation (B.19) becomes

$$v = \left[\frac{\frac{\hbar}{2Mi} \left(f e^{-i\phi} \right) \left(\nabla f e^{i\phi} + i f \nabla \phi e^{i\phi} \right)}{f e^{-i\phi} f e^{i\phi}} \right] - \left[\frac{\frac{\hbar}{2Mi} \left(f e^{-i\phi} \right) \left(\nabla f e^{i\phi} + i f \nabla \phi e^{i\phi} \right)}{f e^{-i\phi} f e^{i\phi}} \right] \quad (\text{B.22})$$

$$v = \frac{\frac{\hbar}{2Mi} \left[f(\nabla f + i f \nabla \phi) e^{-i\phi} e^{i\phi} - f(\nabla f - i f \nabla \phi) e^{-i\phi} e^{i\phi} \right]}{f^2 e^{-i\phi} e^{i\phi}} \quad (\text{B.23})$$

$$v = \frac{\frac{\hbar}{2Mi} \left[f(\nabla f + i f \nabla \phi) - f(\nabla f - i f \nabla \phi) \right]}{f^2} \quad (\text{B.24})$$

$$v = \frac{\hbar}{2Mi} \left[\frac{2i f^2 \nabla \phi}{f^2} \right] \quad (\text{B.25})$$

which becomes

$$v(\mathbf{r}, t) = \frac{\hbar}{M} \nabla \phi(\mathbf{r}, t) \quad (\text{B.26})$$

Equation (B.26) shows that the motion of the condensate corresponds to potential flow, since the velocity is the gradient of a scalar quantity. This is the velocity distribution.

B.2 Rotating frame velocity distribution

The GPE equation is given by

$$i\hbar \frac{\partial \Psi^{(R)}}{\partial t} = -\frac{\hbar^2}{2M} \nabla^2 \Psi^{(R)} + V^{(R)}(\mathbf{r}) \Psi^{(R)} + i\hbar \Omega_z \frac{\partial \Psi^{(R)}}{\partial \Phi} + gN |\Psi^{(R)}|^2 \Psi^{(R)} \quad (\text{B.27})$$

the complex conjugate of equation (B.27) is

$$-i\hbar \frac{\partial \Psi^{*(R)}}{\partial t} = -\frac{\hbar^2}{2M} \nabla^2 \Psi^{*(R)} + V^{(R)}(\mathbf{r}) \Psi^{*(R)} - i\hbar \Omega_z \frac{\partial \Psi^{*(R)}}{\partial \Phi} + gN |\Psi^{(R)}|^2 \Psi^{*(R)} \quad (\text{B.28})$$

multiplying equation (B.27) by $\Psi^{*(R)}$ and equation (B.28) by $\Psi^{(R)}$

$$i\hbar \Psi^{*(R)} \frac{\partial \Psi^{(R)}}{\partial t} = -\frac{\hbar^2}{2M} \Psi^{*(R)} \nabla^2 \Psi^{(R)} + \Psi^{*(R)} V^{(R)}(\mathbf{r}) \Psi^{(R)} + i\hbar \Omega_z \Psi^{*(R)} \frac{\partial \Psi^{(R)}}{\partial \Phi} + gN |\Psi^{(R)}|^2 \Psi^{(R)} \Psi^{*(R)} \quad (\text{B.29})$$

$$-i\hbar \Psi^{(R)} \frac{\partial \Psi^{*(R)}}{\partial t} = -\frac{\hbar^2}{2M} \Psi^{(R)} \nabla^2 \Psi^{*(R)} + \Psi^{(R)} V^{(R)}(\mathbf{r}) \Psi^{*(R)} - i\hbar \Omega_z \Psi^{(R)} \frac{\partial \Psi^{*(R)}}{\partial \Phi} + gN |\Psi^{(R)}|^2 \Psi^{*(R)}(\mathbf{r}) \Psi^{(R)} \quad (\text{B.30})$$

subtract equation (B.30) from equation (B.29)

$$i\hbar \left(\Psi^{*(R)} \frac{\partial \Psi^{(R)}}{\partial t} + \Psi^{(R)} \frac{\partial \Psi^{*(R)}}{\partial t} \right) = \frac{\hbar^2}{2M} \left(\Psi^{(R)} \nabla^2 \Psi^{*(R)} - \Psi^{*(R)} \nabla^2 \Psi^{(R)} \right) + i\hbar \Omega_z \left(\Psi^{*(R)} \frac{\partial \Psi^{(R)}}{\partial \Phi} + \Psi^{(R)} \frac{\partial \Psi^{*(R)}}{\partial \Phi} \right) \quad (\text{B.31})$$

$$i\hbar \frac{\partial}{\partial t} \left(\Psi^{*(R)} \Psi^{(R)} \right) = -\nabla \cdot \frac{\hbar^2}{2M} \left(\Psi^{*(R)} \nabla \Psi^{(R)} - \Psi^{(R)} \nabla \Psi^{*(R)} \right) + i\hbar \Omega_z \left(\Psi^{*(R)} \frac{\partial \Psi^{(R)}}{\partial \Phi} + \Psi^{(R)} \frac{\partial \Psi^{*(R)}}{\partial \Phi} \right) \quad (\text{B.32})$$

Now note that in Cartesian

$$\begin{aligned} \hat{L}_z \left(\Psi^{*(R)} \Psi^{(R)} \right) &= \frac{\hbar}{i} \frac{\partial}{\partial \Phi} \left(\Psi^{*(R)} \Psi^{(R)} \right) \\ &= \left(y \hat{p}_x - x \hat{p}_y \right) \left(\Psi^{*(R)} \Psi^{(R)} \right) \\ &= \frac{\hbar}{i} \left(y \frac{\partial}{\partial x} - x \frac{\partial}{\partial y} \right) \left(\Psi^{*(R)} \Psi^{(R)} \right) \\ &= \frac{\partial}{\partial x} \left(\frac{\hbar}{i} y \Psi^{*(R)} \Psi^{(R)} \right) + \frac{\partial}{\partial y} \left(\frac{\hbar}{i} x \Psi^{*(R)} \Psi^{(R)} \right) \end{aligned} \quad (\text{B.33})$$

we can write now equation (B.33) as the divergence of

$$\begin{aligned}
& -i\hbar y \Psi^{*(R)} \Psi^{(R)} (\mathbf{r}) \hat{\mathbf{i}} + i\hbar x \Psi^{*(R)} \Psi^{(R)} \hat{\mathbf{j}} \\
& = i\hbar (y \hat{\mathbf{i}} - x \hat{\mathbf{j}}) \Psi^{*(R)} \Psi^{(R)} \\
& = i\hbar \rho (\hat{\mathbf{i}} \sin \Phi - \hat{\mathbf{j}} \cos \Phi) \\
& = -i\hbar \rho \Phi(\phi) \Psi^{*(R)} \Psi^{(R)}
\end{aligned} \tag{B.34}$$

so,

$$\frac{\hbar}{i} \left(y \frac{\partial}{\partial x} - x \frac{\partial}{\partial y} \right) \Psi^{*(R)} \Psi^{(R)} = \nabla \cdot \left(-i\hbar \rho \Phi(\phi) \Psi^{*(R)} \Psi^{(R)} \right) \tag{B.35}$$

so, inserting equation (B.35) into equation (B.32) gives

$$\begin{aligned}
& i\hbar \frac{\partial}{\partial t} \left(\Psi^{*(R)} \partial \Psi^{(R)} \right) = \\
& -\nabla \cdot \frac{\hbar^2}{2M} \left(\Psi^{*(R)} \nabla \Psi^{(R)} - \Psi^{(R)} \nabla \Psi^{*(R)} \right) -
\end{aligned} \tag{B.36}$$

$$\begin{aligned}
& i\hbar \Omega_z \frac{\partial}{\partial \Phi} \left(\Psi^{*(R)} \Psi^{(R)} \right) \\
& i\hbar \frac{\partial}{\partial t} \left(\Psi^{*(R)} \partial \Psi^{(R)} \right) = \\
& -\nabla \cdot \left[\frac{\hbar^2}{2M} \left(\Psi^{*(R)} \nabla \Psi^{(R)} - \Psi^{(R)} \nabla \Psi^{*(R)} \right) - \right. \\
& \left. -i\hbar \rho \Omega_z \Phi(\phi) \Psi^{*(R)} \Psi^{(R)} \right]
\end{aligned} \tag{B.37}$$

$$\begin{aligned}
& \frac{\partial}{\partial t} \left(\Psi^{*(R)} \partial \Psi^{(R)} \right) + \\
& \nabla \cdot \left[\frac{\hbar^2}{2M} \left(\Psi^{*(R)} \nabla \Psi^{(R)} - \Psi^{(R)} \nabla \Psi^{*(R)} \right) - \right. \\
& \left. -\rho \Omega_z \Phi(\phi) \Psi^{*(R)} \Psi^{(R)} \right] = 0
\end{aligned} \tag{B.38}$$

defining the rotating frame density and the probability density current

$$\rho^{(R)} = \Psi^{*(R)} \Psi^{(R)} \tag{B.39}$$

$$\mathbf{J}^{(R)} = \frac{\hbar^2}{2M} \left(\Psi^{*(R)} \nabla \Psi^{(R)} - \Psi^{(R)} \nabla \Psi^{*(R)} \right) - \rho \Omega_z \Phi(\hat{\phi}) \Psi^{*(R)} \Psi^{(R)} \quad (\text{B.40})$$

which satisfy the rotating frame continuity equation

$$\frac{\partial \rho^{(R)}}{\partial t} + \nabla \cdot \mathbf{J}^{(R)} = 0 \quad (\text{B.41})$$

now define the rotating frame velocity distribution as

$$\mathbf{J}^{(R)} = \rho^{(R)} \mathbf{v}^{(R)} \quad (\text{B.42})$$

or

$$\mathbf{v}^{(R)} = \frac{\mathbf{J}^{(R)}}{\rho^{(R)}} \quad (\text{B.43})$$

thus

$$\mathbf{v}^{(R)} = \frac{\hbar}{2Mi} \left(\frac{\Psi^{*(R)} \nabla \Psi^{(R)} - \Psi^{(R)} \nabla \Psi^{*(R)}}{\Psi^{*(R)} \Psi^{(R)}} \right) - \rho \Omega_z \Phi(\hat{\phi}) \quad (\text{B.44})$$

Smooth flow has already been produced by stirring ring-shaped BECs both theoretically [51] and experimentally [1]. Since the racetrack becomes ring if the length L , of the straightways is set to zero, we are encouraged to try making smooth flow in this racetrack atom circuit.